BNIP3 attenuates hepatocellular carcinoma by promoting lipid droplet turnover at the lysosome.

Damian Berardi
The University of Chicago https://orcid.org/0000-0002-4734-5634
Althea Bock-Hughes
The University of Chicago https://orcid.org/0000-0002-5544-9740
Lauren Drake
The University of Chicago https://orcid.org/0000-0002-2022-5894
Alexander Terry
UIC https://orcid.org/0000-0003-4731-8537
Grazyna Bozek
The University of Chicago
Kay Macleod (kmacleod@uchicago.edu)
The University of Chicago https://orcid.org/0000-0002-8995-4155

Article

Keywords: hepatic steatosis, lipid accumulation, tumor cell growth

Posted Date: October 11th, 2021

DOI: https://doi.org/10.21203/rs.3.rs-947988/v1

BNIP3 attenuates hepatocellular carcinoma by promoting lipid droplet turnover at the lysosome.

Key words: BNIP3, mitochondria, lipogenesis

Running title: BNIP3 is a tumor suppressor in liver

Damian E. Berardi[1], Althea Bock-Hughes[1, 2], Lauren E. Drake[1], Alexander Terry[1], Grazyna Bozek[1] & Kay F. Macleod[1, 2, 3, 4]

1 The Ben May Department for Cancer Research
The Gordon Center for Integrative Sciences, W-338
The University of Chicago
929 E 57th Street, Chicago IL 60637

2 The Committee on Molecular Metabolism and Nutrition
The University of Chicago

3 The Committee on Cancer Biology
The University of Chicago

4 *Corresponding author*
Tel: 773-834-8309
Fax: 773-702-4476
E-mail: kmacleod@uchicago.edu

Abstract

Hepatic steatosis is a major etiological factor in hepatocellular carcinoma (HCC). Work reported here identifies BNIP3 as a suppressor of HCC that mitigates against lipid accumulation. Loss of BNIP3 decreased tumor latency and increased tumor burden in a mouse model of HCC. This was associated with increased lipid accumulation and elevated HCC tumor cell growth. Conversely, exogenous BNIP3 decreased lipid levels and reduced HCC tumor cell growth. Mutant BNIP3^{W18A} that is unable to promote mitophagy did not decrease HCC cell growth and was defective at reducing lipid levels. Growth suppression by BNIP3 was not mediated by effects on fatty acid oxidation (FAO) or *de novo* lipogenesis (DNL). Rather, BNIP3 suppressed HCC cell growth by promoting lipid droplet turnover at the lysosome through a process we have termed “mitolipophagy” in which lipid droplets and mitochondria are turned over together at the lysosome. Low BNIP3 expression in human HCC also correlated with increased lipid content and worse prognosis than HCC expressing high levels of BNIP3. This work reveals a role for BNIP3 and lipid droplet turnover at the lysosome in attenuating HCC.

Introduction

The increasing incidence of hepatocellular carcinoma (HCC) in individuals with non-alcoholic fatty liver disease (NAFLD) and non-alcoholic steatohepatitis (NASH) points to obesity, and to fatty liver in particular [1-4], as a major etiological factor in HCC in western society [5-10]. Indeed, the relative risk of mortality from liver cancer was shown to be significantly elevated (1.5- to 4-fold) amongst obese patients compared to non-obese individuals, more than for any other human cancer studied [5,11,12]. Given the continuing increase in morbid obesity in the US population [1,10,11], efforts to understand how fatty liver promotes HCC are likely to be highly significant in terms of identifying biomarkers predictive of disease onset or progression, in addition to finding novel targets for therapy.

Pioneering work from the Karin lab has shown obesity driven inflammation to be a major contributing factor in the progression of NASH to HCC [13-15] but defects in lipid homeostasis that cause cell death and inflammation in the liver leading to HCC are not fully understood. Altered mitochondrial function has been reported in human NASH and NAFLD [16,17] and could contribute to altered lipid metabolism in a variety of ways, such as changes in rates of fatty acid oxidation (FAO), export of citrate to the cytosol for lipid synthesis, and production of metabolic intermediates and mitochondrial reactive oxygen species (ROS) that affect lipid species produced [18]. Independent of lipid metabolism, dysfunctional mitochondria also modulate production of pro-inflammatory signals, as well as the type and extent of cell death that contributes to tumor progression [19]. Mitochondrial function is maintained in part through the turnover of dysfunctional and/or excess mitochondria at the autolysosome by mitophagy [20]. BNIP3 is a mitochondrial cargo receptor that is induced in the liver by nutrient stress [21] and interacts directly with processed LC3 to target mitochondria for degradation at the autolysosome thereby contributing to metabolic zonation in the liver [22].

Here we examined a novel role for BNIP3 in liver tumorigenesis where we show that targeted deletion of *Bnip3* in a mouse model of HCC caused reduced tumor latency and increased tumor growth rate that was associated with increased lipid content in tumors at earlier stages of disease. BNIP3 decreased HCC growth rates by increasing rates of lipid droplet (LD) turnover at the lysosome in a modified form of lipophagy that we have termed “mitolipophagy” in which LDs get turned over in association with BNIP3-expressing mitochondria. Low BNIP3 expression in human HCC also correlated high lipid content and worse overall survival.

Results

Loss of Bnip3 reduces HCC tumor latency and promotes HCC tumor growth.

To examine the role of BNIP3 in hepatocellular carcinoma (HCC), we injected 15 day old *Bnip3*$^{+/+}$ and *bnip3*$^{-/-}$ mice with the chemical carcinogen diethylnitrosamine (DEN) that is known to induce HCC with predicted latency in laboratory mice [23,24]. We harvested mice at 24, 32 and 40 weeks of age to assess the effect of *Bnip3* loss on both latency and growth of HCC. At 24 weeks of age, macroscopic liver lesions were apparent on the surface of the *bnip3*$^{-/-}$ liver (Fig. 1a, top right, arrows) but not on the *Bnip3*$^{+/+}$ liver. By 40 weeks of age, large tumors were obvious on both the *Bnip3*$^{+/+}$ and *bnip3*$^{-/-}$ livers, although the lesions on the *bnip3*$^{-/-}$ liver were visibly larger than those in *Bnip3*$^{+/+}$ liver (Fig. 1a). Quantification of tumor number (total per liver on serial sections through each liver) and tumor size (diameter) supported the visual assessment that tumors form earlier and grow faster in DEN-treated *bnip3*$^{-/-}$ mice than wild-type mice. Specifically, by 24 weeks of age, there were significantly more tumors detected in the DEN-treated *bnip3*$^{-/-}$ mice than in DEN-treated wild-type control mice (Fig. 1b) although by 32 and 40 weeks of age, the difference in tumor number was no longer significant (Fig. 1b). By contrast, for those tumors that were detectable at 24 weeks, there was no significant difference in tumor size between wild-type and *bnip3*$^{-/-}$ mice initially but by 32 and 40 weeks, the *bnip3*$^{-/-}$ tumors were significantly larger than those forming in wild-type mice (Fig. 1c). In summary, loss of *Bnip3* reduces tumor latency and increases tumor growth rate of DEN-induced HCC in mice.

Interestingly, when we examined BNIP3 expression by immunohistochemistry in tumors forming in wild-type mice, we noted that BNIP3 expression is elevated in HCC tumors (T) at 24 weeks compared to adjacent normal (N) liver (Fig. 1d). By contrast, BNIP3 levels were lower in HCC tumors (T) compared to adjacent normal liver (N) at 32 weeks and 40 weeks (Fig. 1d). The upregulation of BNIP3 in HCC tumors at 24 weeks compared to adjacent normal liver, is likely mediated by elevated nuclear Hif1α expression which is also elevated in HCC tumors at 24 weeks (Supp. Fig. 1). qPCR showed that *Bnip3* mRNA isolated from primary tumor and adjacent normal tissue was down-regulated in tumors at 32 weeks and 40 weeks of age (Fig. 1e) suggesting that loss of BNIP3 expression in wild-type HCC at later timepoints is likely mediated by gene silencing since *Bnip3* mRNA levels are decreased (Fig. 1e) despite persistent expression of nuclear Hif1α (Supp. Fig. 1). Consistent with RNA expression analysis, most HCC tumors at 32 weeks and all tumors at 40 weeks showed decreased BNIP3 protein levels, compared to levels in adjacent normal liver (Fig. 1f). These results show that while BNIP3 is expressed at higher levels in early-stage HCC lesions than in adjacent normal liver, there is selection for loss of endogenous *Bnip3* expression as wild-type tumors progress to later stages of hepatocellular tumorigenesis.

Loss of Bnip3 is associated with increased lipid accumulation in HCC.

In addition to loss of BNIP3 expression in wild-type tumors at 32 to 40 weeks of age, there was also a change in the appearance of HCC tumors forming in wild-type mice. At 24 weeks of age, wild-type HCCs contain small, tightly packed tumor cells, whereas by 32 and 40 weeks of age, HCC tumors contained larger tumor cells with more "bubbles" suggesting increased lipid accumulation (Fig. 1d). To assess this, we stained liver sections from wild-type and *bnip3*$^{-/-}$ DEN treated mice with Oil red O (ORO) to determine lipid content in tumors at 24, 32 and 40 weeks (Fig. 2a-c). Consistent with the pattern detected by H&E staining (Fig. 1d; Fig. 2a, top left), we observed that wild-type tumors at 24 weeks contained less lipid compared to surrounding normal tissue (Fig. 2a, middle panel). By contrast, HCC tumors forming in *bnip3*$^{-/-}$ livers contained considerably more lipid at 24 weeks than did tumors in wild-type mice (Fig. 2a) which was apparent by both H&E staining and by ORO staining. However, tumors growing in 40 week old wild-type mouse liver that had lost Bnip3 expression (Fig. 1d-f), exhibited higher lipid content than surrounding normal liver and as high as that detected in *bnip3*$^{-/-}$ tumors (Fig. 2b). Quantification of ORO staining confirmed these observations (Fig. 2c). At 24 weeks, there was increased lipid content in *bnip3*$^{-/-}$ tumors compared to wild-type, but these differences in lipid content diminished over time at 32 and 40 weeks, as wild-type tumors lost *Bnip3* expression and simultaneously accumulated more lipid (Fig. 2c). Increased lipid content in *bnip3*$^{-/-}$ HCC was associated with increased transcript levels of genes involved in fatty acid synthesis (Fig. 2d), including fatty acid synthase (*Fasn*), acetyl CoA carboxylase 1 (*Acaca*), ATP citrate lyase (*Acly)* and Stearoyl CoA desaturase-1 (*Scd1*). Immunohistochemistry for ACACA and FASN indicated that HCC tumors at 24 weeks in both *Bnip3*$^{+/+}$ and *bnip3*$^{-/-}$ mice express higher levels of these enzymes than surrounding normal tissue (Fig. 2e-f). In summary, our findings show that loss of *Bnip3* either by genetic deletion in *bnip3*$^{-/-}$ mice, or via silencing at late stages of tumorigenesis in wild-type mice is associated with increased lipid accumulation in HCC.

BNIP3 reverses lipid accumulation in HCC cells and inhibits HCC cell growth.

To gain mechanistic insight to how BNIP3 was modulating lipid content in HCC tumors, we established primary cell lines from different *bnip3*$^{-/-}$ tumors and then generated stable lines using lentiviral vectors expressing either empty vector (EV), HA-tagged wild-type BNIP3 (HA-BNIP3) or HA-tagged BNIP3 mutated at W18 to inhibit LC3 interaction and block mitophagy (HA-BNIP3^{W18A}) [22]. We validated expression of EV, HA-BNIP3 or HA-BNIP3^{W18A} in *bnip3*$^{-/-}$ lines (Fig. 3a) and confirmed expression of alpha-fetoprotein (AFP), an oncofetal protein expressed during liver development and re-expressed in HCC tumors (Fig. 3a). We confirmed that expression of HA-BNIP3, but not EV or HA-BNIP3^{W18A}, promoted mitophagy by staining for overlap between processed LC3B (an autophagosome marker) and TOMM20 (a mitochondrial marker) in the presence of bafilomycin A_1 (Fig. 3b). Exogenous HA-BNIP3 expression decreased staining for TOMM20 and induced significant overlap in LC3B-TOMM20 staining,

whereas EV and HA-BNIP3^{W18A} did not (Fig. 3b). Decreased mitochondrial staining was visible in HA-BNIP3 expressing HCC cells in the presence (Fig. 3b) or absence of bafilomycin A_1 (Supp. Fig. 2a), but the overlap between LC3 and TOMM20 could only be detected in the presence of bafilomycin A_1 (Fig. 3b) indicating that there was increased mitophagic flux when HA-BNIP3 was expressed but not with EV or HA-BNIP3^{W18A} expression. We also noted that HA-BNIP3 induced mitochondrial fragmentation, that was most striking when cells were bafilomycin A_1 treated (Fig. 3b), but not in the absence of bafilomycin A1 (Supp. Fig. 2a). Together these results indicate that BNIP3 promotes mitochondrial fragmentation and preferential mitophagy of these fragmented mitochondria at the autolysosome, which is dependent on its interaction with LC3, since this was not observed in either EV or HA-BNIP3^{W18A} expressing HCC cells.

Mitochondrial mass was also indirectly assessed by qPCR for mitochondrial genome copy number (amplifying for *Nd1* and *Cytb*) relative to nuclear DNA (amplifying beta-hemoglobin/*Hbb*) and shown to be decreased in HCC cells expressing HA-BNIP3 but not EV or HA-BNIP3^{W18A} (Fig. 3c). Also, consistent with decreased mitochondrial mass, we observed decreased oxygen consumption in HCC cells expressing HA-BNIP3 but not EV or HA-BNIP3^{W18A} (Fig. 3d). Interestingly, we observed that exogenous HA-BNIP3 decreased extracellular acidification of growth media following a glycolysis stress test performed using the Seahorse analyzer (Fig. 3e) and suppressed glucose uptake by HCC cells in culture (Fig. 3f). Consistent with these findings *in vitro* and with increased growth rate of HCC lacking *Bnip3*, there was increased glucose uptake into HCCs in *bnip3*$^{-/-}$ liver compared to *Bnip3*$^{+/+}$ liver as measured by FDG-PET analysis of live mice at 32 weeks of age (Supp. Fig. 3). Overall, these results show that exogenous HA-BNIP3, but not EV or HA-BNIP3^{W18A}, promotes mitophagy and reduces mitochondrial mass in HCC cells. In addition, BNIP3 reduces reliance on glucose to fuel either OXPHOS or glycolysis.

Given the steatotic phenotype *in vivo* in HCC tumors growing in the absence of BNIP3, we examined lipid content of HCC cells in culture expressing EV, HA-BNIP3 or HA-BNIP3^{W18A} by staining cells with the lipophilic dye, BODIPY 493/503. We observed that expressing exogenous HA-BNIP3 decreased the number of BODIPY positive lipid droplets in HCC cells compared to EV control expressing HCC cells (Fig. 4a – 4c). Intriguingly, even though HA-BNIP3^{W18A} was unable to promote mitophagy, we observed that this mutant form of BNIP3 retained ability to decrease lipid droplet number compared to EV (Fig. 4a-b). However, when we challenged these cells with oleic acid to further increase cellular lipid content, HA-BNIP3 was significantly more effective at decreasing lipid droplet number than either EV or HA-BNIP3^{W18A} (Fig. 4a, 4c). Nevertheless, HA-BNIP3^{W18A} retained partial ability to decrease lipid droplet number suggesting that while mitophagy is involved in how BNIP3 limits lipid accumulation, a second mitophagy-independent role is also at play. We noted that while HA-BNIP3^{W18A} is defective for mitophagy, it retains the ability to induce mitochondrial fragmentation raising the possibility that mitochondrial

fragmentation contributes to how BNIP3 prevents lipid accumulation. Analysis of BODIPY staining of HCC cells by Imagestream flow cytometric analysis confirmed results obtained by immunofluorescence microscopy in showing decreased lipid droplet numbers when HA-BNIP3 was expressed but not EV, and less so with HA-BNIP3^{W18A} (Fig. 4d, 4e). Imagestream analysis also showed HCC cells expressing HA-BNIP3 to be smaller in size that HCC cells expressing EV or HA-BNIP3^{W18A} (Fig. 4d, 4f). Previous work has linked lower mitochondrial mass and function to decreased overall cell size [25,26].

Exogenous expression of HA-BNIP3 in *bnip3*$^{-/-}$ HCC cells also decreased expression of lipogenic genes (*Fasn, Acaca, Acly*) (Fig. 4g). Most interestingly, exogenous HA-BNIP3 markedly slowed down the growth of *bnip3*$^{-/-}$ HCC cells whereas EV and HA-BNIP3^{W18A} did not (Fig. 4h). In summary, BNIP3 induced mitochondrial fragmentation and mitophagy, decreased lipid accumulation and decreased growth of HCC cells in culture.

BNIP3 promotes fatty acid oxidation but this does not explain how BNIP3 decreases lipid levels or inhibits tumor cell growth.

Lipid accumulation in cells can arise for various reasons, including decreased fatty acid oxidation (FAO) [27] and since FAO takes place in the mitochondrial matrix, we postulated that BNIP3 may be promoting lipid turnover by increasing FAO. To examine this, we measured oxygen consumption in HCC cells expressing EV, HA-BNIP3 or HA-BNIP3^{W18A} using palmitate as a substrate for oxidation (Fig. 5a-e). Given that exogenous HA-BNIP3 decreased mitochondrial mass (Fig. 3b, 3c) and lowered oxidation of glucose in *bnip3*$^{-/-}$ cells (Fig. 3d), we were surprised to observe that HA-BNIP3 markedly increased FAO of palmitate in *bnip3*$^{-/-}$ HCC cells compared to EV or HA-BNIP3^{W18A} (Fig. 5a). HA-BNIP3 expressing HCC cells were also more sensitive to etomoxir (ETO) which suppresses carnitine palmitoyl transferase-1 (CPT1) and blocks fatty acid uptake into the mitochondria to suppress FAO (Fig. 5b, Fig. 5d). Indeed, ETO collapsed oxygen consumption by HA-BNIP3 expressing HCC cells using palmitate as substrate, down to levels seen in HCC cells expressing EV or HA-BNIP3^{W18A} (Fig. 5b, 5d). By contrast ETO had no effect on HCC cells expressing EV or HA-BNIP3^{W18A} (Fig. 5c, 5e). These results suggest that HA-BNIP3 is promoting FAO and thus we were interested to determine if this explained how HA-BNIP3 was able to promote lipid turnover in HCC cells.

Using similar approaches to those described above, we examined whether inhibiting FAO with ETO inhibited the ability of HA-BNIP3 to decrease numbers of BODIPY-positive lipid droplets in HCC cells. Surprisingly, even in the presence of ETO that clearly disrupted FAO, HA-BNIP3 retained the ability to decrease lipid droplet content in HCC cells, even when FAO was inhibited (Fig. 5f, 5g). This ability was also still evident in HCC cells fed oleic acid in the presence of ETO (Fig. 5f, 5h), suggesting that while HA-BNIP3 does indeed promote FAO, HA-BNIP3 has a second activity that regulates lipid droplet content

in HCC cells. Significantly, HA-BNIP3^{W18A} was also able to decrease lipid droplet number in the presence of Etomoxir (Fig. 5f, Fig. 5g), even though this form of BNIP3 was unable to promote FAO of palmitate (Fig. 5b, Fig. 5e). Again, this effect of BNIP3^{W18A} was overcome when cells were fed oleic acid to increase lipid droplet content such that it was clearly less effective than wild-type BNIP3 at promoting lipid droplet clearance (Fig. 5f, Fig. 5g).

Expression of certain genes involved in FAO were modestly increased in HCC cells expressing HA-BNIP3 compared to either EV expressing or HA-BNIP3^{W18A} expressing cells (Fig. 5i) but again, since effects on FAO do not appear to explain the ability of BNIP3 to decrease lipid levels in cells, it is unclear what the significance of the increased expression of CPT2, ACADM and ACADL are for cell growth. Indeed, treatment of HA-BNIP3 expressing HCC cells with ETO had no effect on cell growth (Fig. 5j). These results show that while BNIP3 inhibits FAO in *bnip3*$^{-/-}$ HCC cells, this does not explain how BNIP3 promotes decreased lipid content or how BNIP3 suppresses HCC cell growth.

BNIP3 does not decrease lipid levels or HCC cell growth via effects on lipogenesis.

To assess whether BNIP3 was decreasing lipid content in HCC cells by inhibiting *de novo* lipogenesis, we examined the effect of treating cells with an active site inhibitor of FASN called TVB-3664 that is active on mouse cells [28]. Treatment of cells for 24 hours with TVB-3664 markedly increased expression of fatty acid synthesis genes (*Fasn, Acaca, Acly*) irrespective of genotype (Fig. 6a), as expected due to transcriptional feedback effects when lipid synthesis is repressed [29]. Inhibiting FASN is expected to increase cellular levels of malonyl CoA that gets depleted as a substrate for FASN to make palmitate. Interestingly, only cells expressing HA-BNIP3, not EV or HA-BNIP3^{W18A}, showed increased malonyl CoA when treated with the TVB-3664 FASN inhibitor (Fig. 6b). This suggests that FASN was more active in HA-BNIP3 expressing HCC cells than cells expressing either EV or HA-BNIP3^{W18A}, consistent with there being lower lipid levels in cells expressing HA-BNIP3. In addition to acting as a substrate for FASN, malonyl CoA also inhibits FAO by preventing carnitine uptake by CPT1 [30]. Similar to the effects of ETO on FAO, and consistent with increased malonyl CoA produced by FASN inhibition in HA-BNIP3 expressing cells, we observed that TVB-3664 inhibited FAO of palmitate in HA-BNIP3 expressing HCC cells (Fig. 6d) compared to EV (Fig. 6c) or HA-BNIP3^{W18A} expressing cells (Fig. 6e). Thus, TVB-3664 inhibits both lipid synthesis and FAO in HA-BNIP3 expressing *bnip3*$^{-/-}$ HCC cells.

When we examined the effect of TVB-3664 on lipid content of HCC cells, we observed that it eliminated lipid content almost completely independent of BNIP3 since it decreased lipid content in cells expressing EV, HA-BNIP3 or HA-BNIP3^{W18A} to undetectable levels (Fig. 6f, Fig. 6h). However, by increasing the amount of lipid in cells by feeding them with oleic acid, we observed that HA-BNIP3, but not EV or HA-BNIP3^{W18A}, remained able to decrease lipid content even when FASN (and FAO) was

inhibited (Fig. 6g, Fig. 6h), arguing that the ability of BNIP3 to decrease lipid content in HCC cells was independent of effects on DNL and/or FAO. Furthermore, the repressive effect of FASN inhibition on growth of HA-BNIP3 expressing cells was synergistic with the effect of exogenous HA-BNIP3 (Fig. 6i) suggesting that BNIP3 is suppressing tumor cell growth in a manner independent of lipid synthesis. In addition, TVB-3664 inhibition of FASN was also able to inhibit growth of EV and HA-BNIP3^{W18A} expressing HCC cells (Fig. 6i), consistent with the growth suppressive effects of TVB-3664 being BNIP3-independent. In summary, while TVB-3664 inhibits HCC cell growth, this is independent of BNIP3 and BNIP3 (but not EV or BNIP3^{W18A}) suppresses HCC cell growth independently of TVB-3664 and FASN activity. Thus far, we have excluded the effects of BNIP3 on FAO or DNL as explaining how BNIP3 decreases lipid levels and attenuates HCC tumor cell growth.

BNIP3 limits lipid content and HCC cell growth by promoting lipid droplet turnover.

Another mechanism by which cells regulate lipid content is via turnover of lipid droplets (LDs) that involves both lipolysis and lipophagy. LDs are a means of storing triacylglycerides, stearyl esters and retinyl esters within a phospholipid membrane and LDs play important roles in the regulation of fatty acid trafficking within the cell [31]. LD turnover relies on cytosolic lipases, such as adipose triglyceride lipase (ATGL) while the engulfment of LDs by autophagosomes in a process known as lipophagy, relies on acid lipases at the lysosome [32-34]. LDs are known to associate with mitochondria [35-37] and given the role of BNIP3 in mitophagy, we examined a potential role for BNIP3 in promoting LD turnover via a mechanism that integrates mitophagy with lipophagy. When we inhibited lysosomal lipases with Lalistat2 (LALi) [33], we observed increased numbers of LDs accumulating in HCC cells when HA-BNIP3 was expressed but less with EV or HA-BNIP3^{W18A} (Fig. 7a, 7b) suggesting that BNIP3 relied on lysosomal lipases to elicit at least part of its effect in decreasing LD numbers. ImageStream analysis confirmed that LALi only increased BODIPY LD number significantly when HA-BNIP3 was expressed and less so when HA-BNIP3^{W18A} or EV was expressed (Supp. Fig. 4a, 4b). Interestingly, LALi appeared to increase LD numbers but did not increase overall cell size of HCC cells expressing HA-BNIP3, (Supp. Fig. 4a, 4c) indicating that reduced HCC cell size with HA-BNIP3 was not likely due to effects of BNIP3 on LD numbers. In summary, these results suggested to us that BNIP3 was decreasing lipid content in HCC cells by promoting LD turnover at the lysosome.

To examine this more carefully, we co-stained cells for BODIPY and lysotracker to examine overlap of LDs with the lysosome. Experiments were performed in the presence of oleic acid and LALi to allow such structures to accumulate. While a few overlapping LD/lysosomes were detected in EV and HA-BNIP3^{W18A} expressing HCC cells (Fig. 7c), there was a marked increase in overlap (white) between BODIPY (green) and Lysotracker (magenta) in HCC cells expressing HA-BNIP3 (Fig. 7c). Notably,

smaller green LDs were seen predominantly inside magenta-colored lysosomes while larger LDs did not associate with lysosomes (Fig. 7c). Analysis of LDs, mitochondria and lysosomes in the different HCC lines by transmission electron microscopy (TEM), revealed plentiful LDs in both EV and HA-BNIP3^{W18A} expressing cells (Fig. 7d), and fewer LDs in the HA-BNIP3 expressing HCC cells, consistent with BODIPY imaging of cells showing HA-BNIP3 decreasing LD number. There were also more mitochondria in EV and HA-BNIP3^{W18A} expressing HCC cells (Fig. 7d), supporting conclusions from Fig. 3 that HA-BNIP3, but not EV or HA-BNIP3^{W18A}, promotes mitophagy and lowers mitochondrial mass. Lysosomes were also more evident in HA-BNIP3 expressing cells (Fig. 7d) and contained LD-like structures inside lysosomes (Fig. 7e, middle) as also seen by fluorescence microscopy (Fig. 7e, left) as well as LDs associated with mitochondria (Fig. 7e, right). Taken together, these data suggest that BNIP3 is promoting LD turnover at the lysosome in conjunction with turnover of mitochondria.

Treatment of cells with LALi significantly decreased the growth of HCC cells expressing HA-BNIP3 but had no effect on the growth of cells expressing EV or HA-BNIP3^{W18A} (Fig. 7f), suggesting that BNIP3 suppresses HCC cell growth by promoting lysosomal turnover of LDs in a mitophagy-dependent manner. LALi treatment also decreased palmitate oxidation suggesting that fatty acids liberated by lysosomal lipases are fueling FAO in HCC cells (Fig. 7g). However, this effect was independent of BNIP3 consistent with data described above (Fig. 5) indicating that altered FAO does not explain how BNIP3-dependent LD turnover suppresses cell growth. At this time, it is not clear to us how LDs promote HCC cell growth but LDs could act as reservoirs of phospholipids and other lipids used by growing cancer cells for membrane expansion and other pro-growth functions. In summary, these data indicate that BNIP3 attenuates HCC cell growth by promoting LD turnover by a process we refer to as “mitolipophagy”.

Low BNIP3 expression in human HCC correlates with worse overall survival.

We examined publicly available RNA-Seq data comparing transcript expression in human HCC to healthy human liver tissue [38], that showed expression of genes involved in fatty acid metabolism, cholesterol metabolism and adipogenesis to be up-regulated in HCC compared to healthy liver (Supp. Fig. 5a-c), in line with previously published data [39-41]. When we examined BNIP3 expression in these data-sets, we observed that while lipid synthesis genes like FASN and ACLY were increased in HCC compared to healthy tissue, BNIP3 was significantly decreased (Fig. 8a, 8b). Interestingly, PPARGC1A that promotes mitochondrial biogenesis was also increased in HCC compared to healthy liver while ACADM that promotes FAO was decreased (Fig. 8a). Linear regression analysis showed a highly significant inverse correlation between levels of FASN, ACLY and PPARGC1A and BNIP3 (Supp. Fig. 5d - f) and a direct correlation between ACADM and BNIP3 (Supp. Fig. 5g). These data indicate that in HCC where lipogenic programs are increased, BNIP3 is significantly decreased.

We further explored TCGA data looking at how expression levels of BNIP3 affects overall survival of patients with HCC and showed a correlation between levels of BNIP3, acetyl CoA carboxylase-1 (ACACA) and patient survival. The ACACA gene encodes an enzyme that catalyzes conversion of acetyl CoA to malonyl CoA to promote lipid synthesis, and is frequently up-regulated in human cancers, including HCC [42,43]. Interestingly, we found that high BNIP3 expression levels in combination with high ACACA expression portended a highly significant increase in overall survival rates (Fig. 8c) in contrast to the combination of high ACACA expression with low BNIP3 expression that had the worst prognosis for overall survival (Fig. 8e). Moreover, when we examined the histology of liver sections from these HCC patients, we observed that high BNIP3 mitigated against lipid accumulation linked to high ACACA expression (Fig. 8d) in contrast to low BNIP3 where high levels of lipid were associated with high ACACA expression (Fig. 8f). These results indicate that high BNIP3 expression is associated with decreased lipid accumulation, less aggressive HCC and increased patient survival when linked to high ACACA expression while conversely low BNIP3 predicts increased lipid accumulation and worse patient outcome.

Discussion

Our work identifies a novel role for BNIP3 in limiting HCC by promoting lipid droplet turnover at the lysosome (Fig. 9). This conclusion was reached after first interrogating the role of BNIP3 in rates of fatty acid oxidation (FAO) and also in *de novo* lipogenesis (DNL). FAO in particular seemed likely to be influenced by BNIP3 since it takes place in the mitochondrial matrix. FAO has generally been reported to be required for cancer growth, including in MYC-driven triple negative breast cancer [44], KRAS-driven lung cancer [45] and other cancers [46]. FAO protects tumor cells from cell death induced by loss of attachment (anoikis) [47] and/or under conditions of nutrient deprivation [48]. In these conditions, FAO-dependent generation of ATP for energy, NADH to feed the electron transport chain, acetyl CoA to prime the TCA cycle and NADPH (via TCA-derived citrate) to mitigate against ROS levels, have all been cited as explaining the pro-tumorigenic function of FAO [49]. To our surprise, BNIP3 very potently promoted FAO in HCC cells using palmitate as a substrate (Fig. 5d) whereas mitophagy-defective BNIP3^{W18A} was unable to promote FAO (Fig. 5e) indicating that the strong effect of BNIP3 on FAO was mitophagy-dependent. Mitochondrial fission is known to precede mitophagy [50,51] and indeed, BNIP3 induces both mitochondrial fragmentation and mitophagy [52]. Thus, one possible explanation for how BNIP3 promotes FAO is by promoting the turnover of smaller more fragmented mitochondria, thereby increasing the cellular proportion of fused mitochondria. Fused mitochondria are more efficient at FAO [53], possibly due to more efficient exchange of reducing agents and metabolic intermediates within the mitochondrial matrix [54]. Nevertheless, this effect of BNIP3 in promoting FAO is unlikely to explain HCC growth suppression since inhibition of FAO with Etomoxir failed to block the growth suppressive properties of BNIP3 (Fig. 5j).

Increased rates of *de novo* lipogenesis (DNL) have also been linked to increased tumorigenesis, including HCC and other cancers [43,55], and indeed SNPs associated with the FASN, ACACA and ACLY genes predict disease outcome including recurrence of human HCC [56]. Increased lipid synthesis may promote tumor cell growth by fueling triglyceride formation for cell membranes and signaling, amongst other functions [27]. Interestingly, breast cancer cells are particularly dependent on fatty acid synthesis after metastasizing to the brain which has limited fatty acid availability compared to either the primary site or other metastatic sites [57]. These studies have driven efforts to target FASN and ACACA enzymes for therapeutic benefit [43,55,58-60]. However, our work shows that the ability of BNIP3 to promote lipid clearance from HCC tumor cells, was not dependent on rates of lipogenesis since BNIP3 could decrease lipid levels robustly even in the presence of an effective FASN inhibitor (Fig. 6h).

Having excluded effects of BNIP3 on FAO and DNL as explaining how BNIP3 decreased both lipid droplet (LD) number and HCC cell growth, we considered the possibility that BNIP3 was promoting lipolysis of neutral lipids contained in LDs. Inhibiting lysosomal acid lipases with Lalistat2 (LALi) significantly attenuated the inhibitory effect of BNIP3 on LD number (Fig. 7a) suggesting that BNIP3 is

somehow promoting lipophagy in which lipid droplets are turned over at the lysosome [32]. This became more interesting when, unlike FAO and DNL inhibitors, we also observed a marked decrease in the ability of BNIP3 to limit HCC tumor cell growth following treatment with LALi (Fig. 7f). Using LALi to inhibit turnover of LDs that had been taken up by lysosomes, we observed that BNIP3 promoted increased LD uptake by lysosomes compared to either EV or BNIP3^{W18A}, but also that it was the smallest LDs that were taken up by the lysosome (Fig. 7c). Larger LDs appeared to be resistant to turnover at the lysosome. As discussed above, mitophagy is preceded by mitochondrial fragmentation and there is preferential turnover of smaller mitochondria causing larger more fused mitochondria to predominate [50,51]. Mitochondria and LDs associate with each other through various mechanisms [35,36], and LD size is partly determined by surface area of contact with peri-droplet mitochondria [61]. LD size increases in proportion to the size of the mitochondria with which it associated [61]. Conversely, smaller lipid droplets associate with smaller mitochondria that in turn are more susceptible to turnover at the autolysosome.

Thus, to reconcile our collective findings, we suggest that BNIP3 promotes LD turnover through "mitoplipophagy" in which small LDs get turned over with associated smaller, fragmented mitochondria (Fig. 9). Selective forms of autophagy imply that only the selected cargo gets turned over and certainly upregulation of specific cargo receptors like BNIP3 promote increased mitophagy preferentially over other selective forms of autophagy. However, analysis of electron micrographs clearly indicates that while mitochondria make up the bulk of the cargo during mitophagy, other organelles, such as associated ER and ribosomes also get turned over by association with targeted mitochondria [62]. Indeed, our TEM revealed interactions between fragmented mitochondria and lipid droplets inside membrane bound vesicles (Fig. 7e), consistent with our suggestion that BNIP3 limits lipid accumulation by promoting LD turnover with associated mitochondria. This BNIP3-dependent tumor suppressive mechanism may be unique to liver where accumulating lipid promotes both NAFLD and NASH, and progression to HCC, and ongoing studies are examining the extent to which BNIP3 modulates lipid content in other tissues and tumor types, and whether this contributes to the growth suppressive effect of BNIP3.

Methods

Mice

All mice (wild-type and *bnip3*$^{-/-}$ mice) were maintained on a pure C57Bl/6J genetic background. Mice were maintained in an environmentally controlled specific pathogen free barrier facility and provided *ad libitum* with water and chow. Tumors were induced in mice by intra-peritoneal injection of 15 day old male mice with 25 mg/kg diethylnitrosamine (DEN).

Cells

Primary hepatocellular carcinoma cell lines were established from *bnip3*$^{-/-}$ mice using a standard two-step liver perfusion technique, as described previously by our lab [22]. Macroscopic tumors evident in the excised and collagenase perfused liver were dissected away from surrounding non-tumor liver parenchyma in a culture dish containing isolation media (DMEM/4.5 g/l glucose, 1 mM lactate, 2 mM L-glutamine, 15 mM Hepes, 100 nM dexamethasone, 10 % defined fetal bovine serum (Hyclone), 100 U/ml penicillin/0.1 mg/ml streptomycin). Tumors were disaggregated by pipetting, filtered through a 75 μm filter and washed three times in isolation media. The HCC cell pellet was resuspended in defined HCC growth media (DMEM/F12, 10% defined fetal bovine serum (Hyclone), 100 nM dexamethasone, 20 μg/l epidermal growth factor, 1x Insulin-Transferrin-Selenium (ITS, Gibco, Cat# 41400045), 100 U/ml penicillin/0.1 mg/ml streptomycin). HCC cell lines were expanded and infected overnight in the presence of 8 μg/ml polybrene with lentivirus (pLVX) expressing either empty vector sequences (EV), HA-BNIP3 or HA-BNIP3^{W18A}, and selection for expressing lines was performed in 200 μg/ml hygromycin. Cell lines were validated for exogenous BNIP3 expression by western blot with α-HA, α-AFP and by immunofluorescence for HA (see below). Experiments were conducted in HCC defined media (no hygromycin) in the presence or absence of 100 μM BSA-conjugated oleic acid (Sigma cat# O3008). Drug treatments included 10 μM Etomoxir (Sigma cat# 509455) for 24 hours, 12 nM TVB-3664 (3V-Biosciences) for 24 hours, 20 μM Atglistatin (ATGLi) (Cayman Chemical, cat# 15284) for 24 hours, or 50 μM Lalistat2 (LALi) (Cayman Chemical, cat# 25347) for 24 hours.

Analysis of Oxygen Consumption Rates

HCC cells were seeded in Seahorse XF96 microplates at a density of 0.75 x 10^4 cells/well. The next day, the cellular mitochondrial stress test was performed according to the manufacturer's protocol (1 μm oligomycin; 0.75 μm FCCP; 5 μM Antimycin A), using the Seahorse XF96 analyzer in the Biophysics Core at the University of Chicago. Briefly, 2X DMEM base media was used to make 1X DMEM

supplemented with 4.5 g/L glucose, 2mM glutamine, and 1mM sodium pyruvate, with a pH adjusted to 7.35. Cells were rinsed with PBS prior to addition of 175uL of 1X DMEM and the plate was incubated in the absence of CO_2 for approximately 1 hour. Alternatively, cells were incubated in substrate-limited growth media for 24h and then palmitate was added as the main carbon source according to the manufacturer's protocol in the palmitate oxidation stress kit from Agilent Plc, cat# 103693-100). Data were normalized by cell number using Hoechst 33342 nuclear counterstain and fluorescence quantification using a microplate reader. Normalized OCR data was then analyzed using Agilent Seahorse Wave software.

Measurement of Cell Growth Rate.

HCC that stably express HA-BNIP3 or HA-BNIP3W18A or Empty Vector as control were seeded into twelve wells each per condition (8*104 cells per well) on 96 well plates. Cells were treated or not with different drugs (TVB-3664, Etomoxir or LALi) and confluence was measured along the time with the IncuCyte Live-Cell Analysis System (Sartorius) over a 7 day period.

RNA extraction

Cells in a 6-well plate were washed twice with 2mL of DPBS followed by addition of 1mL Trizol. Wells were incubated for 5 minutes at RT and collected in eppendorf tubes. At this step, samples could be frozen at -80 °C or immediately extracted for RNA. For extraction, 200uL of chloroform was added to each sample, followed by vigorous shaking for 15 seconds and incubation for 3 minutes at RT. Tubes were centrifuged at 12,000xg, 15 min, at 4 °C. The aqueous upper phase (~400 µL) was transferred into a fresh tube, followed by addition of 1 volume of 70% EtOH (~400uL) and vigorous shaking. Samples were incubated for 5 minutes and then applied to RNeasy columns. The remainder of the extraction was performed according to the RNeasy Mini kit protocol (Qiagen) and included on-column DNaseI digestion. RNA was eluted in 50 µL of RNase-free water, concentrations were measured using the NanoDrop Spectrophotometer, and samples were stored at -80 °C.

Quantitative PCR

To make cDNA, 1-2 µg of RNA was reverse transcribed using the High Capacity RNA-to-cDNA kit (Applied Biosystems). The concentration of cDNA was measured by NanoDrop and samples were stored at -20 °C. For gene expression analysis, we performed quantitative real-time PCR on 250 ng of cDNA

per sample using Taqman gene-specific fluorogenic probes (Applied Biosystems/Thermo Fisher). Primers used for qPCR included in this manuscript are as follows:

Genomic copy number (Mt:Nuc gDNA):

Cyba: Mm00241140_cn
Ndufa1: Mm00526370_cn
Hbb-bh1: Mm00216612_cn

Gene expression:
Bnip3: Mm01275601_g1
Fasn: Mm01253292_m1
Acaca:Mm01304277_m1
Acly: Mm00652520_m1
Scd1: Mm00772290_m1
Cpt1a: Mm00550438_m1
Cpt2: Mm00487205_m1
Acadm: Mm01323360_g1
Acadl: Mm00599660_m1
Rps12: Mm03030276_g1

Immunohistochemistry & Oil Red O staining

Immunohistochemistry on mouse liver sections was carried out as described previously [22] using heat denaturation in citrate buffer pH 6.0 to expose epitope. Stained slides were digitized using an Allied Vision Technologies Stingray F146C color slide scanner and quantified using the Spectrum Plus Image analysis software (Aperio). Antibodies were used in IHC as follows: Ki67 (Labvision, cat# RM9106), α-BNIP3 (Sigma Prestige, HPA003015) 1:100; α-FASN (Cell Signaling Technology, cat# 3180) 1: 100; α-ACACA (Cell Signaling Technology, cat# 3676) 1: 200. Oil Red O staining was performed on frozen liver sections that were warmed to room temperature, fixed for 10 minutes in cold 10% neutral buffered formalin and allowed to air dry. Slides were incubated in propylene glycol for 3 minutes and then in Oil Red O/propylene glycol solution for 10 minutes, followed by 3 minutes in 85% propylene glycol and washing three times in water. Oil Red O reagents were obtained from Newcomer Supply (Cat.# 9119A). Oil Red O stained sections were then counterstained in hematoxylin and mounted using Vectashield (Vector Laboratories). Oil red O droplets were quantified in the red channel following deconvolution and thresholding, using Image J (NIH).

Protein extraction

For harvesting of cells, plates were washed in ice-cold DPBS followed by scraping in 1mL of DPBS containing protease inhibitors (0.5 mM PMSF, 1 µg/mL aprotinin, 1 µg/mL leupeptin, 1 mM Na_3VO_4). Cells were pelleted at 3000xg for 3 minutes at 4°C and resuspended in RIPA lysis buffer (10 mM Tris-HCl pH 8.0, 150 mM NaCl, 1% sodium deoxycholate, 0.1% SDS, 1% Trition X-100) containing

protease and phosphatase inhibitors (Roche PhosSTOP inhibitor cocktail tablet). Samples were incubated on ice for 15 minutes with vortexing every 5 minutes, and centrifuged at full speed for 15 minutes at 4 °C. The supernatant was transferred to pre-chilled Eppendorf tubes and protein concentration was measured on a NanoDrop spectrophotometer and stored frozen at -80 °C.

Western blot

Protein samples were denatured by boiling for 5 min with SDS reducing sample buffer (400 mM Tris pH 6.8, 10% SDS, 500 mM β-mercaptoethanol) and sample loading dye (60% glycerol and bromophenol blue). The amount of protein loaded per sample varied depending on the proteins being probed, but typically 75 µg was loaded onto SDS-PAGE gels, followed by transfer to nitrocellulose (0.2 µm pore, GE Healthcare) or PVDF (0.45 µm pore, GE Healthcare) membranes. Membranes were blocked in 5% nonfat milk in TBS/0.05% Tween (TBST) for 30 minutes at room temperature with shaking and incubated with primary antibodies overnight at 4 °C on a rocker, in 5% BSA/TBST for antibodies from Cell Signaling Technology and in 5% nonfat milk/TBST for all others. The next day, membranes were washed 3 times with TBST and incubated with HRP-conjugated secondary antibody (Dako) in 5% nonfat milk/TBS-T for 2 hours at room temperature on a shaker. Membranes were washed 3 times in TBS-T and proteins were visualized by chemiluminescence and exposure on X-ray film. Antibodies for western blots were used as follows: α-HA (Cell Signaling 3724) 1:2,000, α-BNIP3 (Cell Signaling #3769) 1:500, α-Alpha fetoprotein (Santa Cruz sc-15375) 1:500.

Immunofluorescence & confocal microscopy

For immunofluorescence staining, cells were seeded onto 8 well chambered coverslips (Ibidi #80826) and grown in HCC growth media. Cells were treated with Bafilomycin A_1 (Enzo Cat#: BML-CM110) at 100nM for the last 4hr of the experiment. At experimental endpoint, media was aspirated and wells washed in DPBS followed by fixation in 4% paraformaldehyde (PFA) (Alfa Aesar cat#: J61899AP) for 15 minutes at RT, followed by permeabilization in ice-cold 100% methanol for 10 minutes at -20°C. Wells were washed with 0.5% TBST and blocked in 10% goat serum in 0.5% TBST for 30 minutes. Wells were incubated with primary antibodies in 10% goat serum in 0.5% TBST overnight at 4°C. Anti-TOMM20 (Abcam, ab56783, 1:150), anti-LC3B (Cell Signaling, 3868S, 1:200). The next day, wells were washed in 0.5% TBST for 3x5 minutes, followed by incubation in appropriate fluorescent secondary antibodies in 10% goat serum/TBST for 1 hour at RT, protected from light. Wells were washed in 0.5% TBST for 3x5 minutes and mounted with Ibidi mounting medium with DAPI (Ibidi cat#: 50011). For BODIPY staining, wells were treated with the relevant drug, if lysosomal visualization was required, cells were treated with LysoTracker Deep Red (Invitrogen cat#: L12492) at 50nM, 4hr before experimental endpoint. Media was

aspirated and wells washed in DPBS followed by fixation in 4% (PFA) for 10 minutes at RT. Incubated cells in 0.5ug/ml BODIPY 493/503 (Invitrogen cat#: D3922) diluted in DPBS for 25 mins. Washed 3x with DPBS and mounted with Ibidi mounting medium with DAPI. All imaging was performed using the Leica TCS SP8 laser scanning confocal microscope in the Integrated Microscopy Core Facility at the University of Chicago. All images were collected using a 63X oil-immersion objective. 10-15 images representative images were obtained for each well.

ImageJ quantification of Lipid Droplets

Quantification of BODIPY positive lipid droplets was performed in FIJI. An ImageJ macro was written to threshold the images using the "MaxEntropy" algorithm for auto-thresholding and to count the lipid droplets in each image. A separate macro was written to quantify the number of nuclei in each image in order to calculate the average number of LDs per cell.

Measurement of Malonyl CoA

Cells were collected from confluent 15cm plates, scraped in 1ml DPBS and immediately frozen at -20°C. Malonyl CoA levels were measured using a Mouse malonyl coenzyme A ELISA Kit (MyBiosource cat# MBS705127) according to manufacturer's instructions. Values were normalized by total protein levels measured using a Brafdord assay protein quantification kit (Bio-Rad cat# 5000201).

Electron Microscopy

Cells were fixed *in situ* in 2% glutaraldehyde/4% paraformaldehyde for 1 hour at room temperature then gently scraped and pelleted at 900 g. The cell pellet was processed for sectioning and electron microscopy by the Electron Microscopy Core facility at the University of Chicago.

Bioinformatic analysis.

Expression data from dataset GSE84073 was downloaded from the GEO database and BioJupies web application [63] was used to perform bioinformatic analysis of BNIP3 expression and Lipid-Mitochondrial genes between healthy liver samples (GSM2653819 and GSM2653820) vs HCC samples(GSM2653823 and GSM2653824). Linear regression correlation analysis between BNIP3 and FASN, ACLY, PPARGC1A or ACADM was performed using BioVinci (Bioturing, San Diego, CA, USA).

Liver hepatocellular carcinoma (LIHC) patient's survival analysis was performed using cBioPortal [64,65] and data from the TCGA PanCancer Atlas (n = 372 patients). LIHC patients were classified into different groups according to the BNIP3 and ACACA median expression value. By Kaplan–Meier method we

obtained the overall survival and comparison between curves were made by using Log-Rank test. Data obtained from cBioPortal database does not require ethical approval.

Statistics

All statistical analyses were carried out using GraphPad Prism of raw data. The data were analyzed using one-way or two-way ANOVA with Tukey's post-test with a 95% confidence interval for data sets involving single parameters or single groups of data. Other datasets involving comparisons amongst multiple groups used Wilcoxon rank sum analyses with a 95 % confidence interval. Data are shown as the mean ± s.e.m. Values of $p \leq 0.05$ are considered significant. * $p \leq 0.05$; ** $p \leq 0.01$; *** $p \leq 0.001$; **** $p \leq 0.0001$.

Study approval

All work was approved by the University of Chicago Institutional Animal Care and Use Committee under protocols 71155 and 72056.

Author Contributions.

Maintenance and establishment of mouse model: GB, LED, AT; Tumor analysis and characterization: LED, At, KFM; Cell line generation and characterization: DEB, LED, KFM; qPCR: DB, AT, LED; Western blots: DEB, LED; Fluorescence microscopy: ABH; Seahorse analyses: DEB; Flow cytometry: DEB; Incucyte growth assays: DEB; ELISA assays: ABH; Electron microscopy: ABH, KFM; Human TCGA/Bioinformatics analyses: DEB; Study conceptualization: DEB, ABH, KFM; Manuscript preparation: DEB, ABH, KFM; Manuscript review: all authors.

Acknowledgements.

This work was supported by funding from NIH R01 CA200310 (KFM) and NIH T32 CA009594 (KFM for ABH). The authors thank George Kemble and others at 3V-Bioscences for supplying TVB-3664. This work made use of the Human Tissue Resource Center, the Integrated Small Animal Imaging Facility, the Advanced Electron Microscopy Facility and the Digital Light Microscope Facility that are supported by the University of Chicago Comprehensive Cancer Center Support Grant (P30 CA 014599). The authors particularly thank Terri Li, Brian Roman, Yimei Chen and Christine Labno in these core facilities for outstanding technical assistance.

Figure Legends

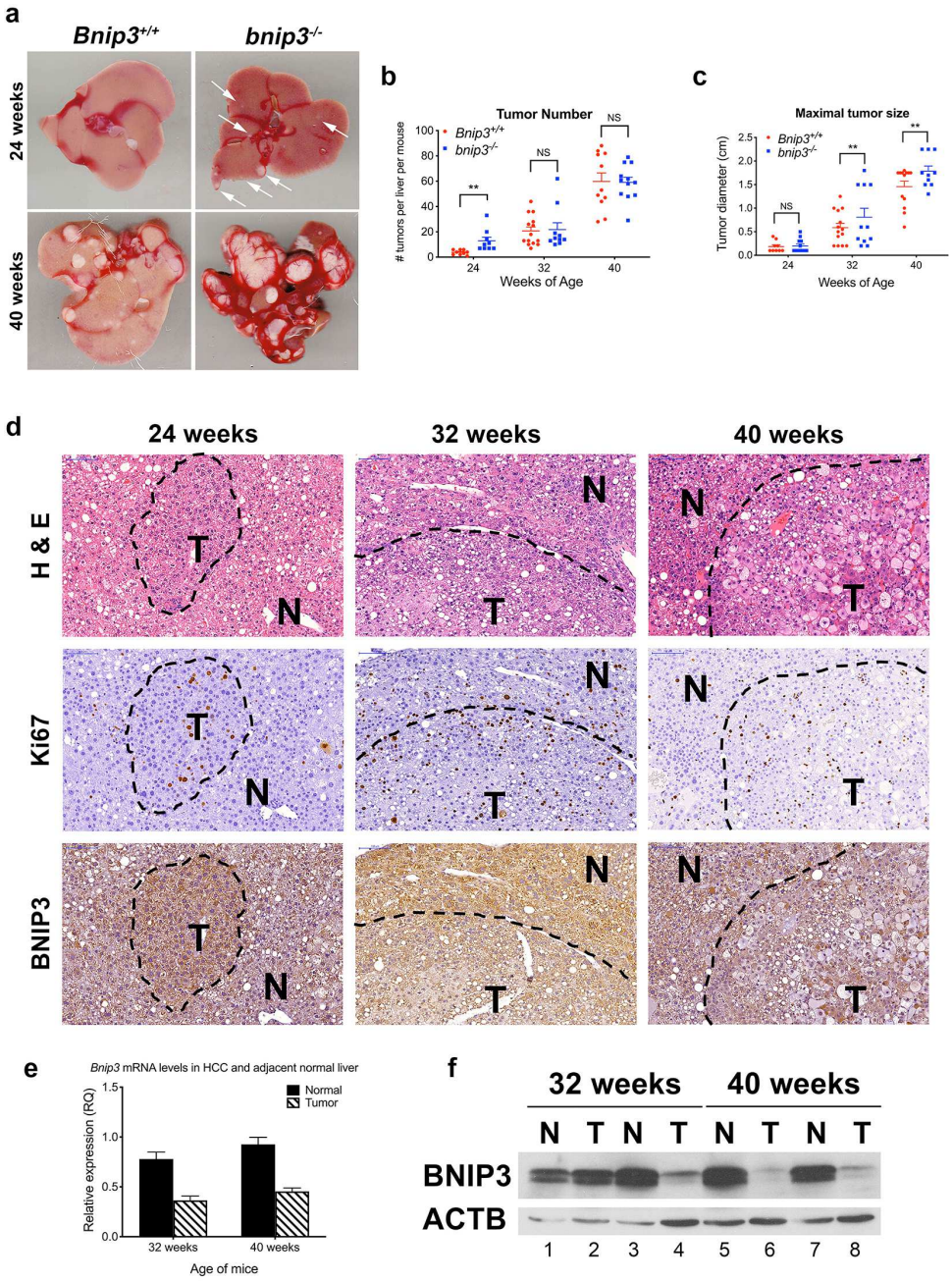

Fig. 1. Loss of BNIP3 promotes HCC initiation and tumor growth. **a** Representative images of HCC tumors forming in the liver of *Bnip3*$^{+/+}$ and *bnip3*$^{-/-}$ mice at 24 weeks and 40 weeks following I.P. injection with 25 mg/kg DEN. **b** Graph of tumor number forming in the liver of *Bnip3*$^{+/+}$ (red) and *bnip3*$^{-/-}$ (blue) mice at 24 weeks and 40 weeks following I.P. injection with 25 mg/kg DEN (NS = not significant, ** = $p < 0.01$). **c** Graph of tumor size in the liver of *Bnip3*$^{+/+}$ (red) and *bnip3*$^{-/-}$ (blue) mice at 24 weeks and 40 weeks following I.P. injection with 25 mg/kg DEN (NS = not significant, ** = $p < 0.01$). **d** Liver sections from *Bnip3*$^{+/+}$ and *bnip3*$^{-/-}$ mice at 24 weeks, 32 weeks and 40 weeks following I.P. injection with 25 mg/kg DEN, stained with hematoxylin & eosin (top row), Ki67 (middle row) and BNIP3 (bottom row). **e** qPCR for *Bnip3* mRNA isolated from HCC lesions and adjacent normal liver in Bnip3$^{+/+}$ mice at 32 weeks and 40 weeks weeks following I.P. injection with 25 mg/kg DEN. **f** Western blot for BNIP3 in protein lysates isolated from HCC tumor lesions (T) and adjacent normal (N) liver in *Bnip3*$^{+/+}$ mice at 32 weeks and 40 weeks weeks following I.P. injection with 25 mg/kg DEN.

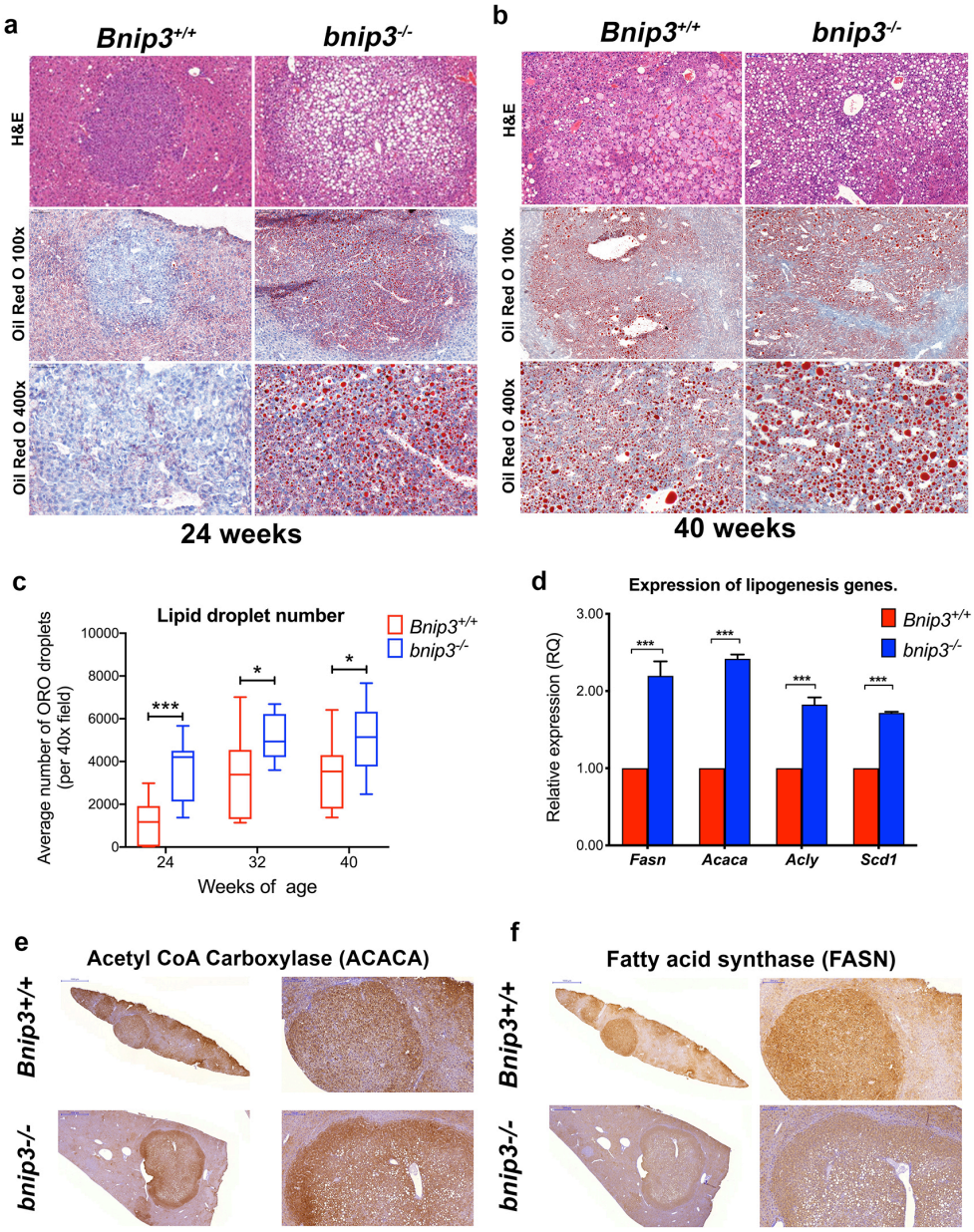

Fig. 2. Lipid increases in HCC when BNIP3 is lost or silenced. **a, b** Liver sections from *Bnip3*$^{+/+}$ and *bnip3*$^{-/-}$ mice at 24 weeks (A) and 40 weeks (B) following I.P. injection with 25 mg/kg DEN, stained with hematoxylin & eosin (top row) or Oil Red O (middle row – 100x magnification, bottom row – 400x magnification). **c** Graph of Oil Red O-positive lipid droplet number in the liver of *Bnip3*$^{+/+}$ (red) and *bnip3*$^{-/-}$ (blue) mice at 24 weeks, 32 weeks and 40 weeks following I.P. injection with 25 mg/kg DEN (NS = not significant, * = $p < 0.05$, *** = $p < 0.001$). **d** qPCR for lipogenic genes Fasn, Acyl, Acaca in tumors from *Bnip3*$^{+/+}$ (red) and *bnip3*$^{-/-}$ (blue) mice at 32 weeks following I.P. injection with 25 mg/kg DEN (*** = $p < 0.001$). **e** Immunohistochemical staining for ACACA in liver sections from *Bnip3*$^{+/+}$ (red) and *bnip3*$^{-/-}$ (blue) mice at 24 weeks following I.P. injection with 25 mg/kg DEN. **f** Immunohistochemical staining for FASN in liver sections from *Bnip3*$^{+/+}$ (red) and *bnip3*$^{-/-}$ (blue) mice at 24 weeks following I.P. injection with 25 mg/kg DEN.

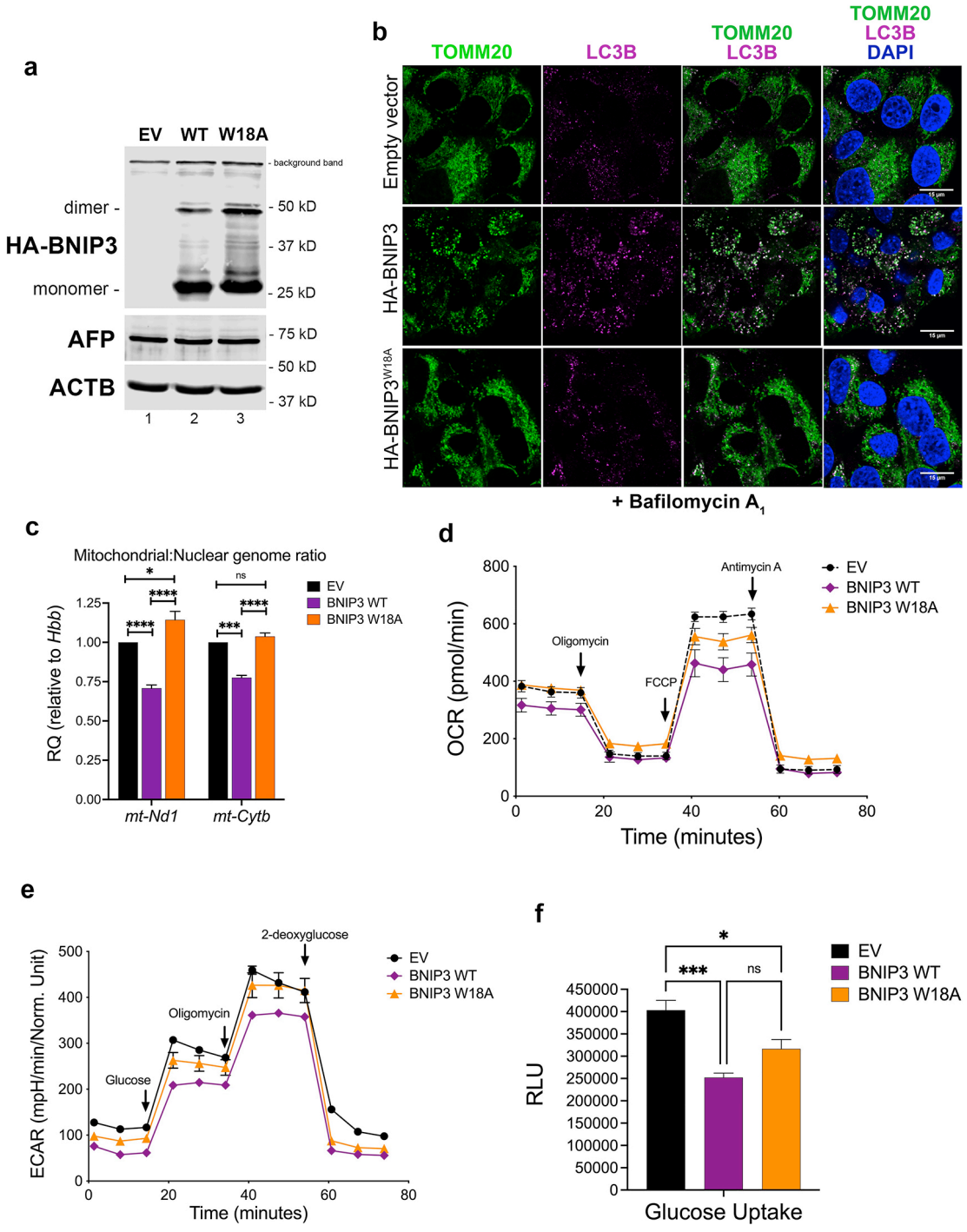

Fig. 3. BNIP3 dependent mitophagy suppresses glucose oxidation, lipid droplet numbers and HCC cell growth. **a** Western blot for α-HA and αFP in protein lysates extracted from *bnip3*$^{-/-}$ HCC cells reconstituted with EV, HA-BNIP3^{WT} or HA-BNIP3^{W18A}. **b** Immunofluorescent staining for TOMM20 and LC3 in *bnip3*$^{-/-}$ HCC cells reconstituted with EV, HA-BNIP3^{WT} or HA-BNIP3^{W18A} in the presence of 100 nM bafilomycin A_1 for 4 hours. **c** qPCR for mt:nuc DNA ratio in *bnip3*$^{-/-}$ HCC cells reconstituted with EV, HA-BNIP3^{WT} or HA-BNIP3^{W18A} (NS = not significant, *** = p < 0.001, **** = p < 0.0001). **d** OCR (glucose) in *bnip3*$^{-/-}$ HCC cells reconstituted with EV, HA-BNIP3^{WT} or HA-BNIP3^{W18A}. **e** ECAR by *bnip3*$^{-/-}$ HCC cells reconstituted with EV, HA-BNIP3^{WT} or HA-BNIP3^{W18A} in a glycolysis stress test performed on the Seahorse XF96 extracellular flux analyzer. **f** Glucose uptake by *bnip3*$^{-/-}$ HCC cells reconstituted with EV, HA-BNIP3^{WT} or HA-BNIP3^{W18A}.

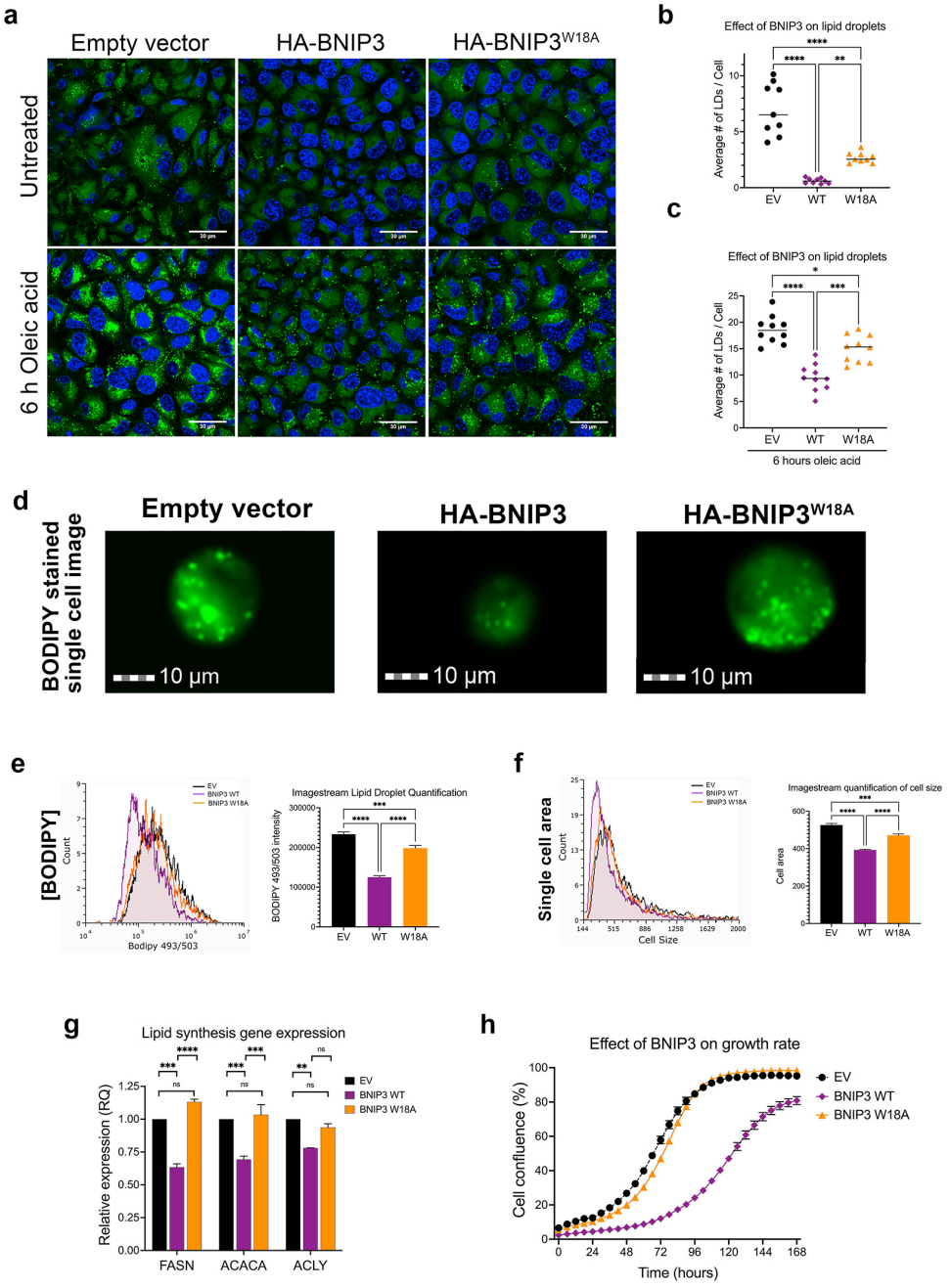

Fig. 4. BNIP3 dependent mitophagy suppresses glucose oxidation, lipid droplet numbers and HCC cell growth. **a** Lipid droplet number (BODIPY 493/503) in *bnip3*$^{-/-}$ HCC cells reconstituted with EV, HA-BNIP3^{WT} or HA-BNIP3^{W18A} +/- oleic acid. **b** Graph of BODIPY 493/503 staining in *bnip3*$^{-/-}$ HCC cells reconstituted with EV, HA-BNIP3^{WT} or HA-BNIP3^{W18A} (***, p < 0.001; ****, p < 0.0001). **c** Graph of BODIPY 493/503 staining in *bnip3*$^{-/-}$ HCC cells reconstituted with EV, HA-BNIP3^{WT} or HA-BNIP3^{W18A} + oleic acid (***, p < 0.001; ****, p < 0.0001). **d** Imagestream analysis of *bnip3*$^{-/-}$ HCC cells reconstituted with EV, HA-BNIP3^{WT} or HA-BNIP3^{W18A} following BODIPY 493/503 staining. **e** Quantification of BODIPY 493/503 Imagestream analysis of *bnip3*$^{-/-}$ HCC cells reconstituted with EV, HA-BNIP3^{WT} or HA-BNIP3^{W18A} (***, p < 0.001, ****, p < 0.0001). **f** Quantification of cell size generated by Imagestream analysis of *bnip3*$^{-/-}$ HCC cells reconstituted with EV, HA-BNIP3^{WT} or HA-BNIP3^{W18A} (***, p < 0.001, ****, p < 0.0001). **g** qPCR for lipid synthesis genes (FASN, ACACA, ACLY) in *bnip3*$^{-/-}$ HCC cells reconstituted with EV, HA-BNIP3^{WT} or HA-BNIP3^{W18A} (NS = not significant, *** = p < 0.001, **** = p < 0.0001). **h** Rate of cell growth determined by IncuCyte of *bnip3*$^{-/-}$ HCC cells reconstituted with EV, HA-BNIP3^{WT} or HA-BNIP3^{W18A}.

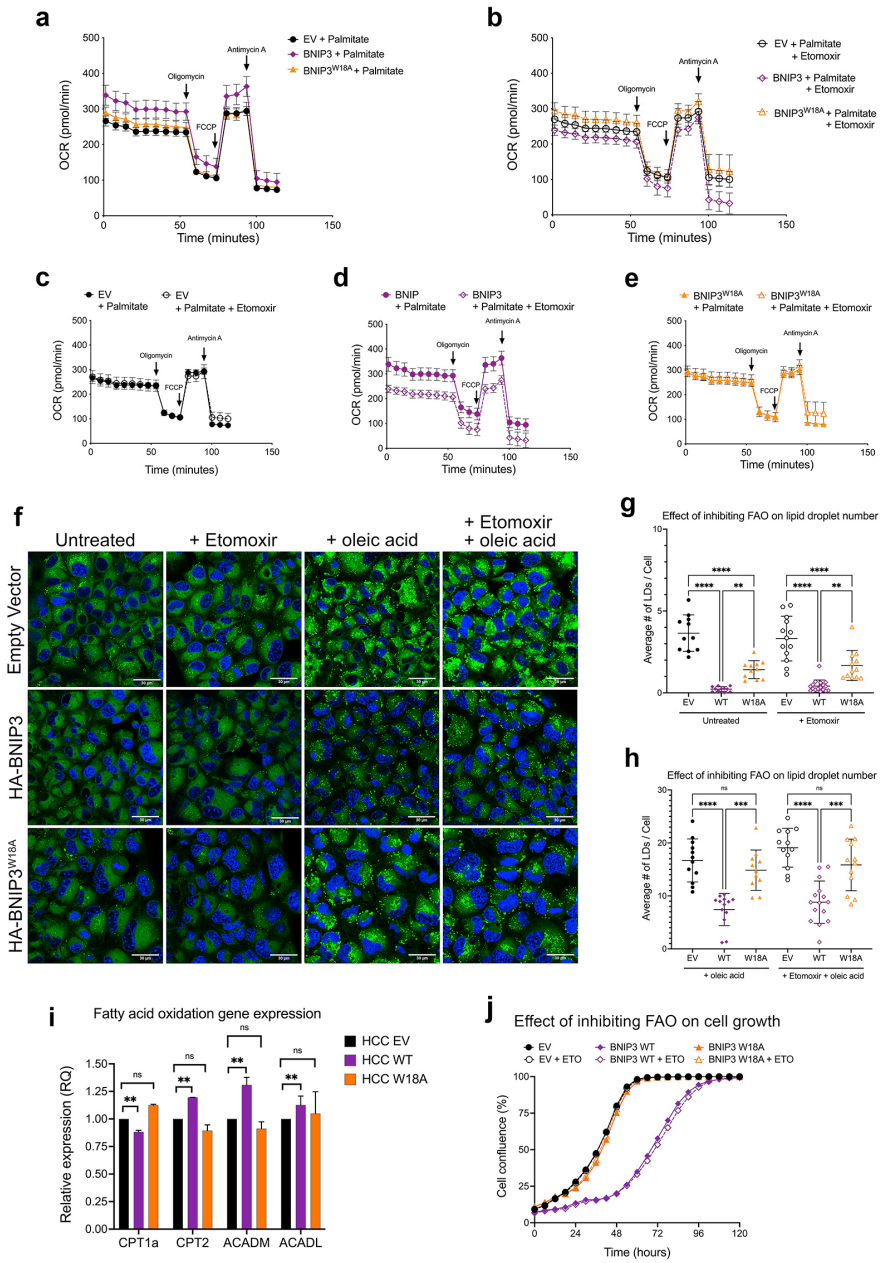

Fig. 5. BNIP3 promotes fatty acid oxidation but this does not explain effects on cell growth. **a** OCR (palmitate) in *bnip3*$^{-/-}$ HCC cells reconstituted with EV, HA-BNIP3^{WT} or HA-BNIP3^{W18A}. **b** OCR (palmitate) in *bnip3*$^{-/-}$ HCC cells reconstituted with EV, HA-BNIP3^{WT} or HA-BNIP3^{W18A} + Etomoxir; **c** OCR (palmitate) in *bnip3*$^{-/-}$ HCC cells reconstituted with EV +/- Etomoxir; **d** OCR (palmitate) in *bnip3*$^{-/-}$ HCC cells reconstituted with BNIP3^{WT} +/- Etomoxir; **e** OCR (palmitate) in *bnip3*$^{-/-}$ HCC cells reconstituted with BNIP3^{W18A} +/- Etomoxir; **f** Fluorescent microscopy imaging of BODIPY 493/503 staining in *bnip3*$^{-/-}$ HCC cells reconstituted with EV, HA-BNIP3^{WT} or HA-BNIP3^{W18A} +/- Etomoxir +/- oleic acid. **g** Graph of BODIPY 493/503 staining in *bnip3*$^{-/-}$ HCC cells reconstituted with EV, HA-BNIP3^{WT} or HA-BNIP3^{W18A} +/- Etomoxir (NS = not significant, *** = p < 0.001, **** = p < 0.0001). **h** Graph of BODIPY 493/503 staining in *bnip3*$^{-/-}$ HCC cells reconstituted with EV, HA-BNIP3^{WT} or HA-BNIP3^{W18A} +/- Etomoxir + oleic acid (NS = not significant, *** = p < 0.001, **** = p < 0.0001). **i** qPCR for FAO genes CPT1a, CPT2, ACADM, ACADL in *bnip3*$^{-/-}$ HCC cells reconstituted with EV, HA-BNIP3^{WT} or HA-BNIP3^{W18A} (NS = not significant, ** = p < 0.01). **j** Rate of cell growth determined by IncuCyte of *bnip3*$^{-/-}$ HCC cells reconstituted with EV, HA-BNIP3^{WT} or HA-BNIP3^{W18A} +/- Etomoxir

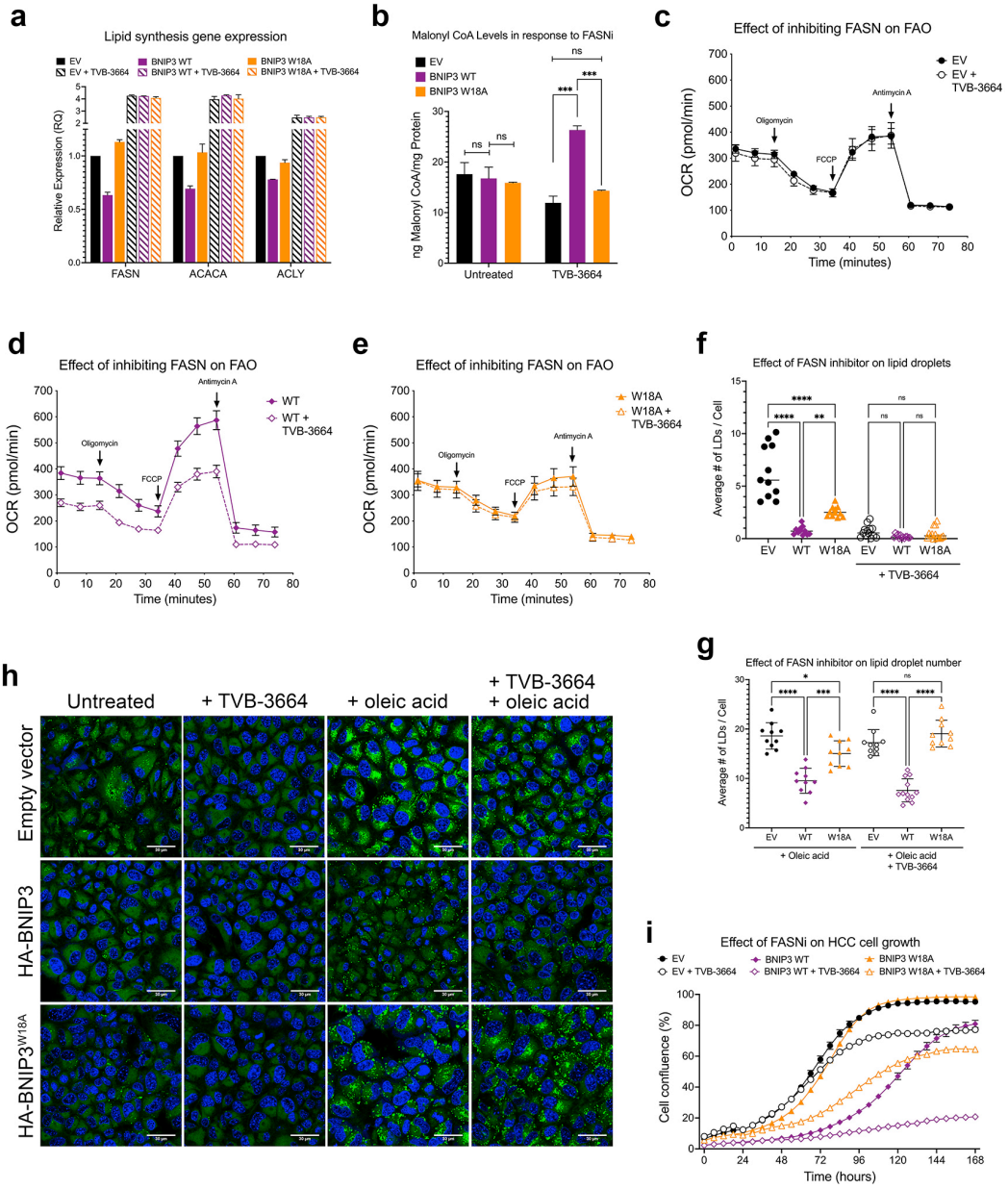

Fig. 6. Inhibiting FASN blocks HCC cell growth but in a BNIP3-independent manner. **a** qPCR for lipogenesis genes FASN, ACLY, ACACA in *bnip3*$^{-/-}$ HCC cells reconstituted with EV, HA-BNIP3^{WT} or HA-BNIP3^{W18A} +/- TVB-3664. **b** Graph of Malonyl CoA levels in *bnip3*$^{-/-}$ HCC cells reconstituted with EV, HA-BNIP3^{WT} or HA-BNIP3^{W18A} +/- TVB-3664 (NS = not significant, *** = $p < 0.001$); **c** Effect of TVB-3664 on OCR (palmitate) in *bnip3*$^{-/-}$ HCC cells reconstituted with EV. **d** Effect of TVB-3664 on OCR (palmitate) in *bnip3*$^{-/-}$ HCC cells reconstituted with HA-BNIP3^{WT}; **e** Effect of TVB-3664 on OCR (palmitate) in *bnip3*$^{-/-}$ HCC cells reconstituted with HA-BNIP3^{W18A}; **f** Graph of BODIPY 493/503 staining in *bnip3*$^{-/-}$ HCC cells reconstituted with EV, HA-BNIP3^{WT} or HA-BNIP3^{W18A} +/- TVB (NS = not significant, ** = $p < 0.01$, **** = $p < 0.0001$); **g** Graph of BODIPY 493/503 staining in *bnip3*$^{-/-}$ HCC cells reconstituted with EV, HA-BNIP3^{WT} or HA-BNIP3^{W18A} +/- Etomoxir + Oleic acid (NS = not significant, * = $p < 0.05$, *** = $p < 0.001$, **** = $p < 0.0001$); **h** Fluorescent microscopy imaging of BODIPY 493/503 staining in *bnip3*$^{-/-}$ HCC cells reconstituted with EV, HA-BNIP3^{WT} or HA-BNIP3^{W18A} +/- TVB-3664 +/- oleic acid; **i** Rate of cell growth determined by IncuCyte of *bnip3*$^{-/-}$ HCC cells reconstituted with EV, HA-BNIP3^{WT} or HA-BNIP3^{W18A} +/- TVB-3664.

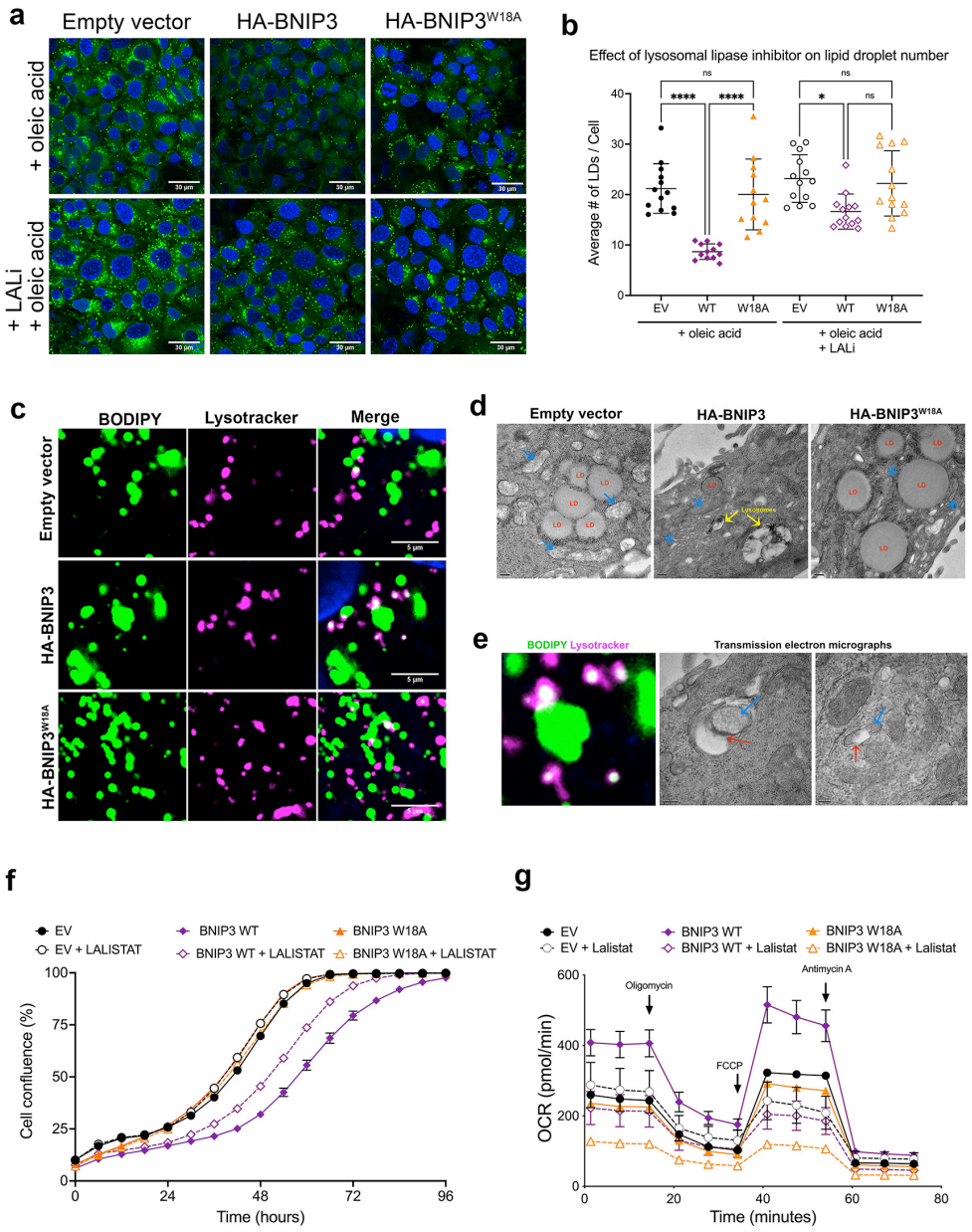

Fig. 7. BNIP3 promotes lipophagy and inhibiting lysosomal lipase limits HCC cell growth. **a** Fluorescent microscopy imaging of BODIPY 493/503 staining in *bnip3*$^{-/-}$ HCC cells reconstituted with EV, HA-BNIP3^{WT} or HA-BNIP3^{W18A} +/- LALi + oleic acid; **b** Graph of BODIPY 493/503 staining in *bnip3*$^{-/-}$ HCC cells reconstituted with EV, HA-BNIP3^{WT} or HA-BNIP3^{W18A} +/- LALi + Oleic acid (NS = not significant, * = $p < 0.05$, ** = $p < 0.01$, **** = $p < 0.0001$); **c** Fluorescent microscopy imaging of BODIPY 493/503 and Lysotracker stained *bnip3*$^{-/-}$ HCC cells reconstituted with EV, HA-BNIP3^{WT} or HA-BNIP3^{W18A} + LALi + oleic acid; **d** TEM on *bnip3*$^{-/-}$ HCC cells reconstituted with EV, HA-BNIP3^{WT} or HA-BNIP3^{W18A} + LALi + oleic acid (red: lipid droplets; blue: mitochondria; yellow: lysosomes); **e** Comparison of fluorescent staining of BODIPY (green) and Lysotracker (magenta) with TEM in *bnip3*$^{-/-}$ HCC cells reconstituted with HA-BNIP3^{WT} showing overlap between mitochondria and lipid droplets. **f** OCR (palmitate) in *bnip3*$^{-/-}$ HCC cells reconstituted with EV, HA-BNIP3^{WT} or HA-BNIP3^{W18A} +/- LALi**; g** Rate of cell growth determined by IncuCyte of *bnip3*$^{-/-}$ HCC cells reconstituted with EV, HA-BNIP3^{WT} or HA-BNIP3^{W18A} +/- LALi.

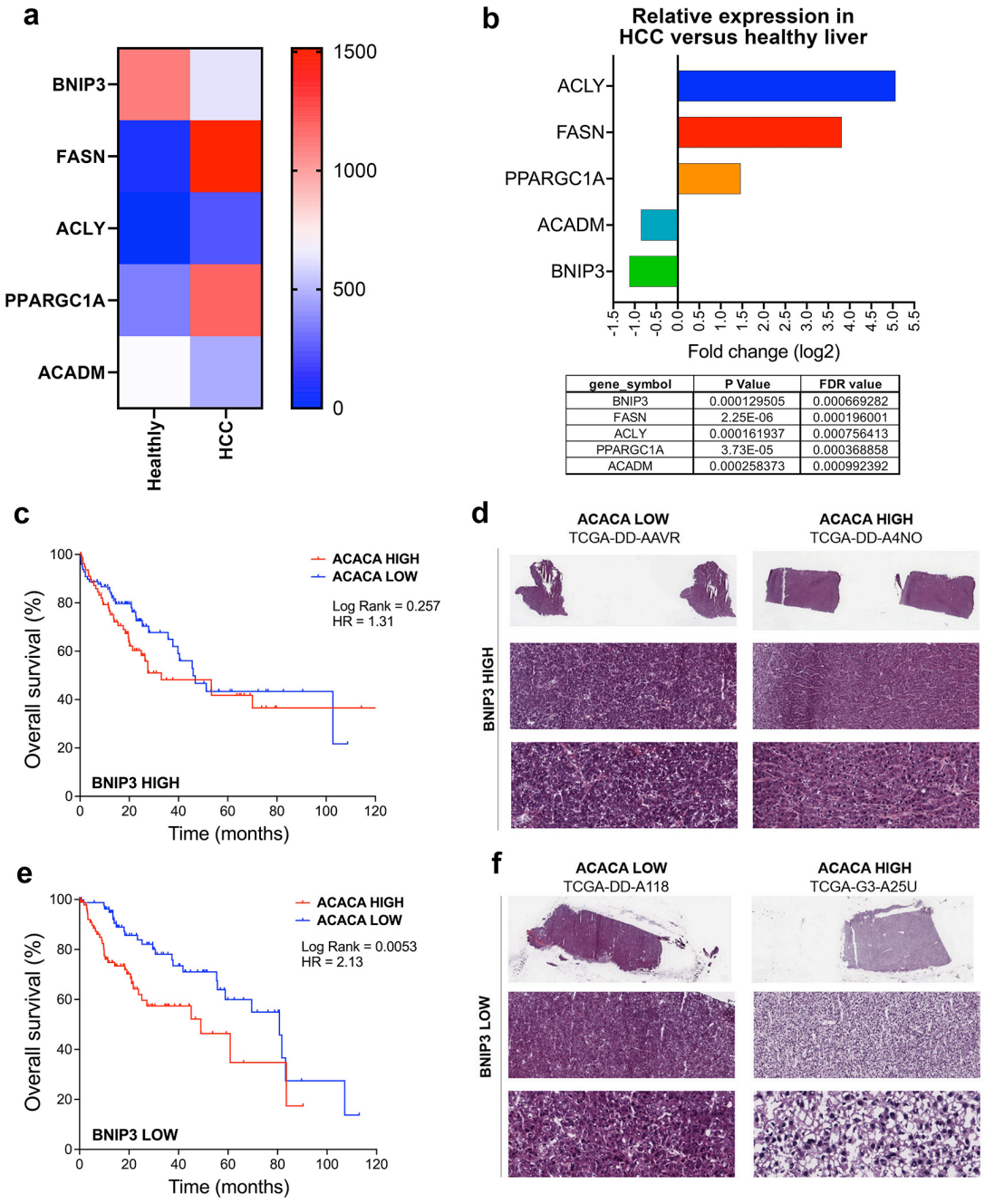

Fig. 8. Low BNIP3 expression in human HCC correlates with high expression of lipogenic genes and poor survival. **a** Comparison of relative expression of BNIP3, FASN, ACLY, PPARGC1A, ACADM in RNA-Seq analysis of healthy liver and HCC. **b** Comparison of the relative effect on levels of BNIP3, FASN and ACLY in healthy liver and HCC. **c** Overall HCC survival data obtained from the TCGA database for tumor showing $BNIP3^{HIGH}$ expression with either $ACACA^{LOW}$ or $ACACA^{HIGH}$ expression. **d** Hematoxylin & eosin stained sections of human $BNIP3^{HIGH}$ -expressing HCC with either $ACACA^{LOW}$ or $ACACA^{HIGH}$ expressing HCC. **e** Overall HCC survival data obtained from the TCGA database for tumor showing $BNIP3^{LOW}$ expression with either $ACACA^{LOW}$ or $ACACA^{HIGH}$ expression. **f** Hematoxylin & eosin stained sections of human $BNIP3^{LOW}$-expressing HCC with either $ACACA^{LOW}$ or $ACACA^{HIGH}$ expressing HCC.

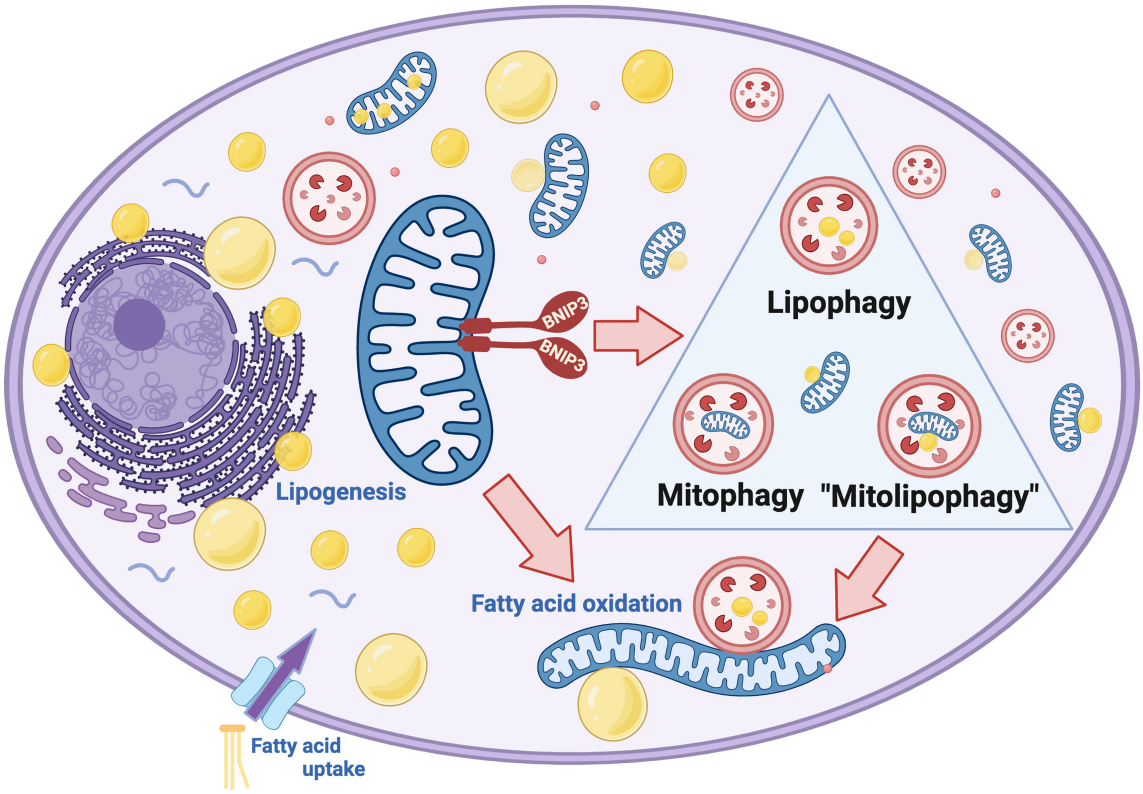

Fig. 9. Diagram summarizing effects of BNIP3 on lipid metabolism in HCC cells.
BNIP3 promotes mitochondrial turnover at the autolysosome (mitophagy) and here we propose that BNIP3-dependent mitophagy also promotes lysosomal turnover of mitochondrial-associated lipid droplets in a process termed “mitolipophagy”, a hybrid form of mitophagy and lipophagy (selective turnover of lipid droplets at the autolysosome). Fatty acids liberated from lipid droplets do fuel fatty acid oxidation in HCC cells but this does not explain the growth suppressive effects of BNIP3 in HCC. Rather we propose that lipid droplets promote tumor growth in other ways, such as serving as a reservoir for lipids to promote plasma membrane growth and organelle biogenesis.

References

1 Cusi, K. Role of obesity and lipotoxicity in the development of nonalcoholic steatohepatitis: pathophysiology and clinical implications. *Gastroenterology* **142**, 711-725.e716, doi:10.1053/j.gastro.2012.02.003 (2012).

2 Sharma, M. *et al.* The Riddle of Nonalcoholic Fatty Liver Disease: Progression From Nonalcoholic Fatty Liver to Nonalcoholic Steatohepatitis. *Journal of clinical and experimental hepatology* **5**, 147-158, doi:10.1016/j.jceh.2015.02.002 (2015).

3 Woo Baidal, J. A. & Lavine, J. E. The intersection of nonalcoholic fatty liver disease and obesity. *Science translational medicine* **8**, 323rv321, doi:10.1126/scitranslmed.aad8390 (2016).

4 Samuel, V. T. & Shulman, G. I. Nonalcoholic Fatty Liver Disease as a Nexus of Metabolic and Hepatic Diseases. *Cell Metab* **27**, 22-41, doi:10.1016/j.cmet.2017.08.002 (2018).

5 Baffy, G., Brunt, E. M. & Caldwell, S. H. Hepatocellular carcinoma in non-alcoholic fatty liver disease: an emerging menace. *Journal of hepatology* **56**, 1384-1391, doi:10.1016/j.jhep.2011.10.027 (2012).

6 Estes, C., Razavi, H., Loomba, R., Younossi, Z. & Sanyal, A. J. Modeling the epidemic of nonalcoholic fatty liver disease demonstrates an exponential increase in burden of disease. *Hepatology* **67**, 123-133, doi:10.1002/hep.29466 (2018).

7 Kanwal, F. *et al.* Risk of Hepatocellular Cancer in Patients With Non-Alcoholic Fatty Liver Disease. *Gastroenterology* **155**, 1828-1837.e1822, doi:10.1053/j.gastro.2018.08.024 (2018).

8 Younossi, Z. *et al.* Nonalcoholic Steatohepatitis Is the Fastest Growing Cause of Hepatocellular Carcinoma in Liver Transplant Candidates. *Clin Gastroenterol Hepatol* **17**, 748-755.e743, doi:10.1016/j.cgh.2018.05.057 (2019).

9 Younossi, Z. M. *et al.* Epidemiology of chronic liver diseases in the USA in the past three decades. *Gut* **69**, 564-568, doi:10.1136/gutjnl-2019-318813 (2020).

10 Loomba, R., Friedman, S. L. & Shulman, G. I. Mechanisms and disease consequences of nonalcoholic fatty liver disease. *Cell* **184**, 2537-2564, doi:10.1016/j.cell.2021.04.015 (2021).

11 Calle, E. E., Rodriguez, C., Walker-Thurmond, K. & Thun, M. J. Overweight, obesity and mortality from cancer in a prospectively studied cohort of US adults. *N. Engl.J.Med.* **348**, 1625-1638 (2003).

12 Larsson, S. C. & Wolk, A. Overweight, obesity and risk of liver cancer: a meta-analysis of cohort studies. *Br. J. Cancer* **97**, 1005-1008 (2007).

13 Park, E. J. *et al.* Dietary and genetic obesity promote liver inflammation and tumorigenesis by enhancing IL-6 and TNF expression. *Cell* **140**, 197-208 (2010).

14 Umemura, A. *et al.* Liver damage, inflammation, and enhanced tumorigenesis after persistent mTORC1 inhibition. *Cell Metab* **20**, 133-144, doi:10.1016/j.cmet.2014.05.001 (2014).

15 Li, X. *et al.* The immunological and metabolic landscape in primary and metastatic liver cancer. *Nat Rev Cancer* **21**, 541-557, doi:10.1038/s41568-021-00383-9 (2021).

16 Brunt, E. M. Nonalcoholic steatohepatitis. *Semin. Liver Dis.* **24**, 3-20 (2004).

17 Begriche, K., Igoudjil, A., Pessayre, D. & Fromenty, B. Mitochondrial dysfunction in NASH: causes, consequences and possible means to prevent it. *Mitochondrion* **6**, 1-28 (2006).

18 Mansouri, A., Gattolliat, C. H. & Asselah, T. Mitochondrial Dysfunction and Signaling in Chronic Liver Diseases. *Gastroenterology* **155**, 629-647, doi:10.1053/j.gastro.2018.06.083 (2018).

19 Font-Burgada, J., Sun, B. & Karin, M. Obesity and Cancer: The Oil that Feeds the Flame. *Cell Metab* **23**, 48-62, doi:10.1016/j.cmet.2015.12.015 (2016).

20 Macleod, K. F. Mitophagy and Mitochondrial Dysfunction in Cancer. *Ann. Rev. Cancer Biol.* **4**, 41 - 60 (2020).

21 Lee, J. M. *et al.* Nutrient-sensing nuclear receptors coordinate autophagy. *Nature* **516**, 112-115 (2014).

22 Springer, M. Z. *et al.* BNIP3-dependent mitophagy promotes cytosolic localization of LC3B and metabolic homeostasis in the liver. *Autophagy*, 1-17, doi:10.1080/15548627.2021.1877469 (2021).

23 Verna, L., Whysner, J. & Williams, G. M. N-nitrosodiethylamine mechanistic data and risk assessment: bioactivation, DNA-adduct formation, mutagenicity, and tumor initiation. *Pharmacol Ther* **71**, 57-81, doi:10.1016/0163-7258(96)00062-9 (1996).

24 Maeda, S., Kamata, H., Luo, J. L., Leffert, H. & Karin, M. IKKb couples hepatocyte death to cytokine-driven compensatory proliferation that promotes chemical hepatocarcinogenesis. *Cell* **121**, 977-990 (2005).

25 Kitami, T. *et al.* A chemical screen probing the relationship between mitochondrial content and cell size. *PloS ONE* **7**, e33755 (2012).

26 Miettinen, T. P. & Björklund, M. Cellular Allometry of Mitochondrial Functionality Establishes the Optimal Cell Size. *Dev Cell* **39**, 370-382, doi:10.1016/j.devcel.2016.09.004 (2016).

27 Snaebjornsson, M. T., Janaki-Raman, S. & Schulze, A. Greasing the Wheels of the Cancer Machine: The Role of Lipid Metabolism in Cancer. *Cell Metab* **31**, 62-76, doi:10.1016/j.cmet.2019.11.010 (2020).

28 Benjamin, D. I. *et al.* Diacylglycerol Metabolism and Signaling Is a Driving Force Underlying FASN Inhibitor Sensitivity in Cancer Cells. *ACS Chem.Biol.* **AOP** (2015).

29 Shimano, H. & Sato, R. SREBP-regulated lipid metabolism: convergent physiology - divergent pathophysiology. *Nature reviews. Endocrinology* **13**, 710-730, doi:10.1038/nrendo.2017.91 (2017).

30 Foster, D. W. Malonyl-CoA: the regulator of fatty acid synthesis and oxidation. *The Journal of clinical investigation* **122**, 1958-1959, doi:10.1172/jci63967 (2012).

31 Welte, M. A. Expanding roles for lipid droplets. *Current biology : CB* **25**, R470-481, doi:10.1016/j.cub.2015.04.004 (2015).

32 Singh, R. *et al.* Autophagy regulates lipid metabolism. *Nature* **458**, 1131-1139 (2009).

33 Schott, M. B. *et al.* Lipid droplet size directs lipolysis and lipophagy catabolism in hepatocytes. *J Cell Biol* **218**, 3320-3335, doi:10.1083/jcb.201803153 (2019).

34 Schulze, R. J. *et al.* Direct lysosome-based autophagy of lipid droplets in hepatocytes. *Proc Natl Acad Sci U S A* **117**, 32443-32452, doi:10.1073/pnas.2011442117 (2020).

35 Freyre, C. A. C., Rauher, P. C., Ejsing, C. S. & Klemm, R. W. MIGA2 Links Mitochondria, the ER, and Lipid Droplets and Promotes De Novo Lipogenesis in Adipocytes. *Molecular cell* **76**, 811-825.e814, doi:10.1016/j.molcel.2019.09.011 (2019).

36 Veliova, M., Petcherski, A., Liesa, M. & Shirihai, O. S. The biology of lipid droplet-bound mitochondria. *Seminars in cell & developmental biology* **108**, 55-64, doi:10.1016/j.semcdb.2020.04.013 (2020).

37 Benador, I. Y., Veliova, M., Liesa, M. & Shirihai, O. S. Mitochondria Bound to Lipid Droplets: Where Mitochondrial Dynamics Regulate Lipid Storage and Utilization. *Cell Metab* **29**, 827-835, doi:10.1016/j.cmet.2019.02.011 (2019).

38 Broutier, L. *et al.* Human primary liver cancer-derived organoid cultures for disease modeling and drug screening. *Nature medicine* **23**, 1424-1435, doi:10.1038/nm.4438 (2017).

39 Yahagi, N. *et al.* Co-ordinate activation of lipogenic enzymes in hepatocellular carcinoma. *Eur J Cancer* **41**, 1316-1322, doi:10.1016/j.ejca.2004.12.037 (2005).

40 Yamashita, T. *et al.* Activation of lipogenic pathway correlates with cell proliferation and poor prognosis in hepatocellular carcinoma. *Journal of hepatology* **50**, 100-110, doi:10.1016/j.jhep.2008.07.036 (2009).

41 Calvisi, D. F. *et al.* Increased lipogenesis, induced by AKT-mTORC1-RPS6 signaling, promotes development of human hepatocellular carcinoma. *Gastroenterology* **140**, 1071-1083, doi:10.1053/j.gastro.2010.12.006 (2011).

42 Svensson, R. U. *et al.* Inhibition of acetyl-CoA carboxylase suppresses fatty acid synthesis and tumor growth of non-small-cell lung cancer in preclinical models. *Nature medicine* **22**, 1108-1119, doi:10.1038/nm.4181 (2016).

43 Lally, J. S. V. *et al.* Inhibition of Acetyl-CoA Carboxylase by Phosphorylation or the Inhibitor ND-654 Suppresses Lipogenesis and Hepatocellular Carcinoma. *Cell Metab* **29**, 174-182.e175, doi:10.1016/j.cmet.2018.08.020 (2019).

44 Camarda, R. *et al.* Inhibition of fatty acid oxidation as a therapy for MYC-overexpressing triple-negative breast cancer. *Nature medicine* **22**, 427-432, doi:10.1038/nm.4055 (2016).

45 Padanad, M. S. *et al.* Fatty Acid Oxidation Mediated by Acyl-CoA Synthetase Long Chain 3 Is Required for Mutant KRAS Lung Tumorigenesis. *Cell reports* **16**, 1614-1628, doi:10.1016/j.celrep.2016.07.009 (2016).

46 Duman, C. *et al.* Acyl-CoA-Binding Protein Drives Glioblastoma Tumorigenesis by Sustaining Fatty Acid Oxidation. *Cell Metab* **30**, 274-289.e275, doi:10.1016/j.cmet.2019.04.004 (2019).

47 Schafer, Z. T. *et al.* Antioxidant and oncogene rescue of metabolic defects caused by loss of matrix attachment. *Nature* **461**, 109-113, doi:10.1038/nature08268 (2009).

48 Zaugg, K. *et al.* Carnitine palmitoyltransferase 1C promotes cell survival and tumor growth under conditions of metabolic stress. *Genes & development* **25**, 1041-1051, doi:10.1101/gad.1987211 (2011).

49 Carracedo, A., Cantley, L. C. & Pandolfi, P. P. Cancer metabolism: fatty acid oxidation in the limelight. *Nat Rev Cancer* **13**, 227-232, doi:10.1038/nrc3483 (2013).

50 Gomes, L. C., Di Benedetto, G. & Scorrano, L. During autophagy mitochondria elongate, are spared from degradation and sustain cell viability. *Nat Cell Biol* **13**, 589-598, doi:10.1038/ncb2220 (2011).

51 Rambold, A. S., Kostelecky, B., Elia, N. & Lippincott-Schwartz, J. Tubular network formation protects mitochondrial from autophagosomal degradation during nutrient starvation. *Proc Natl Acad Sci U S A* **108**, 10190-10195 (2011).

52 Lee, Y. K., Lee, H. Y., Hanna, R. A. & Gustafsson, A. B. Mitochondrial autophagy by Bnip3 involves Drp1-mediated mitochondrial fission and recruitment of Parkin in cardiac myocytes. *Am. j. Physiol. Heart Circ. Physiol.* **301**, H1924-1931 (2011).

53 Rambold, A. S., Cohen, S. & Lippincott-Schwartz, J. Fatty acid trafficking in starved cells: regulation by lipid droplet lipolysis, autophagy, and mitochondrial fusion dynamics. *Dev. Cell* **32**, 678-692 (2015).

54 Rossignol, R. *et al.* Energy substrate modulates mitochondrial structure and oxidative capacity in cancer cells. *Cancer Res.* **64**, 985-993 (2004).

55 Svensson, R. U. & Shaw, R. J. Lipid Synthesis Is a Metabolic Liability of Non-Small Cell Lung Cancer. *Cold Spring Harbor symposia on quantitative biology* **81**, 93-103, doi:10.1101/sqb.2016.81.030874 (2016).

56 Jiang, H. *et al.* Genetic variants in de novo lipogenic pathway genes predict the prognosis of surgically-treated hepatocellular carcinoma. *Scientific reports* **5**, 9536, doi:10.1038/srep09536 (2015).

57 Ferraro, G. B. *et al.* FATTY ACID SYNTHESIS IS REQUIRED FOR BREAST CANCER BRAIN METASTASIS. *Nat Cancer* **2**, 414-428, doi:10.1038/s43018-021-00183-y (2021).

58 Ventura, R. *et al.* Inhibition of de novo Palmitate Synthesis by Fatty Acid Synthase Induces Apoptosis in Tumor Cells by Remodeling Cell Membranes, Inhibiting Signaling Pathways, and Reprogramming Gene Expression. *EBioMedicine* **2**, 808-824, doi:10.1016/j.ebiom.2015.06.020 (2015).

59 Heuer, T. S. *et al.* FASN Inhibition and Taxane Treatment Combine to Enhance Anti-tumor Efficacy in Diverse Xenograft Tumor Models through Disruption of Tubulin Palmitoylation and Microtubule Organization and FASN Inhibition-Mediated Effects on Oncogenic Signaling and Gene Expression. *EBioMedicine* **16**, 51-62, doi:10.1016/j.ebiom.2016.12.012 (2017).

60 Montesdeoca, N., López, M., Ariza, X., Herrero, L. & Makowski, K. Inhibitors of lipogenic enzymes as a potential therapy against cancer. *FASEB journal : official publication of the Federation of American Societies for Experimental Biology* **34**, 11355-11381, doi:10.1096/fj.202000705R (2020).
61 Benador, I. Y. *et al.* Mitochondria Bound to Lipid Droplets Have Unique Bioenergetics, Composition, and Dynamics that Support Lipid Droplet Expansion. *Cell Metab* **27**, 869-885.e866, doi:10.1016/j.cmet.2018.03.003 (2018).
62 Mizushima, N. & Levine, B. Autophagy in mammalian development and differentiation. *Nat. Cell Biol.* **12**, 823-830 (2010).
63 Torre, D., Lachmann, A. & Ma'ayan, A. BioJupies: Automated Generation of Interactive Notebooks for RNA-Seq Data Analysis in the Cloud. *Cell Syst* **7**, 556-561.e553, doi:10.1016/j.cels.2018.10.007 (2018).
64 Cerami, E. *et al.* The cBio cancer genomics portal: an open platform for exploring multidimensional cancer genomics data. *Cancer Discov* **2**, 401-404, doi:10.1158/2159-8290.Cd-12-0095 (2012).
65 Gao, J. *et al.* Integrative analysis of complex cancer genomics and clinical profiles using the cBioPortal. *Sci Signal* **6**, pl1, doi:10.1126/scisignal.2004088 (2013).

Supplementary Files

This is a list of supplementary files associated with this preprint. Click to download.

- SupplementalInformation.pdf
- nrreportingsummaryNCOMMS2138698.pdf